Advancing SeNP synthesis: Innovative confined environments for enhanced stability and size control

Elena Piacenza [a],[*], Filippo Vitale [a], Veronica Ciaramitaro [a], Renato Lombardo [a], Francesco Ferrante [b], Delia F. Chillura Martino [a]

[a] Department of Biological, Chemical, and Pharmaceutical Sciences and Technology (STEBICEF), Università degli Studi di Palermo, Viale delle Scienze, Building 17, 90128, Palermo Italy
[b] Department of Physics and Chemistry - Emilio Segrè, Università degli Studi di Palermo, Viale delle Scienze, Building 17, Palermo Italy

ARTICLE INFO

ABSTRACT

Nanotechnology's exponential growth has spurred a demand for high-quality and safe nanomaterials, prompting increased interest in cost-effective and fast colloidal syntheses that must mitigate their irreversible aggregation, an issue particularly pertaining to spherical selenium nanoparticles (SeNPs), promising materials in a wide array of technological and biological fields.

This study presents a novel approach to SeNP synthesis in confined environments developed from the highly biocompatible surfactant sodium oleate (NaOl) and the amino acid L-cysteine as a selenite-reducing agent. L-cysteine@NaOl (C@NaOl) confined environments were modulable as a function of the amino acid and surfactant concentrations and yielded high-quality spherical SeNPs with enhanced stability. This approach enables generating SeNPs even under alkaline conditions and improving up to 3-fold the final SeNP yield compared to other processes. Besides, we introduce a groundbreaking method for determining SeNP size by adapting Mie's scattering theory to metalloid NPs. This innovative technique proves effective for SeNPs in the 40–100 nm range, offering a reliable alternative to conventional sizing methods. These findings provide valuable insights regarding the generation of bio- and eco-compatible confined environments and SeNPs, paving the way for developing safe, cost-effective, and environmentally friendly strategies for their synthesis with broad applications in various scientific and technological domains.

1. Introduction

Since the 1990s, nanotechnology witnessed a surge in interest derived from the remarkable and unique properties of nanomaterials and their almost infinite applications [1]. The increasing and urgent demand for high-quality nanomaterials has made - and is still making - imperative to develop feasible, reliable, safe, and cost-limited synthetic procedures. In the ever-evolving landscape of nanotechnology, colloidal syntheses satisfy these requirements [2]; yet, attention is needed in these methods to avoid spontaneous and irreversible aggregation of nanomaterials due to their high surface energy and surface-to-volume ratio [3]. Surfactants and polymers help overcome these issues, as their bulky structures exert good steric hindrance and contribute to limiting nanomaterial contact with each other [2,4]. Specifically, charged surfactants or polymers are preferred, as they develop electrostatic repulsion

interactions, conferring electrosteric stabilization to nanomaterials [4, 5]. Besides, these stabilizers often control nanomaterial assembly, size, and morphology [4], behaving like confined environments that enable precisely defining and enhancing their physical-chemical and applicative properties, unlocking new opportunities for tailored nanomaterials.

Among the plethora of nanomaterials available to date, metalloid selenium nanoparticles (SeNPs) are riveting due to their unique physical-chemical attributes, encouraging potential in various scientific and technological domains, biocompatibility, and therapeutic ability [2, 6,7]. These features make SeNPs promising or, in some cases, exceptional materials for biomedicine, renewable energy production, sensor designing, and optoelectronics [2,6]. Spherical SeNPs are conventionally obtained through colloidal syntheses based on the fast and controllable reduction of suitable Se precursors [2] - e.g., sodium selenite (Na_2SeO_3), seleninic acid (H_2SeO_3), or selenium oxide (SeO_2) – with

thiol-containing compounds (glutathione or L-cysteine), hydrazine, acetic acid, oxalic acid, dextrose, or sodium thiosulphate [8,9]. Besides chemical methods, SeNPs are often produced through biological processes, ultrasonic-assisted and hydrothermal syntheses, pulsed laser ablation, or UV-light irradiation [9]. Overall, these methods frequently face crucial challenges, such as pH control, low production yield, use of toxic reagents, long time of synthesis, variability in the biological matrices, need for expensive and high-maintenance instrumentation, high energy consumption, NP polydispersity, and sample pollution [8,9]. Specifically, chemical processes, although generally simple, rapid, and efficient, generate SeNPs with limited stability, culminating in the phase transition of Se within these NPs from amorphous (red) to the thermodynamically stable trigonal (grey) allotrope, which preferentially forms nanorods or microcrystals [2,8]. This phenomenon is usually avoided through stabilizing agents, such as water-soluble synthetic polymers or natural polysaccharides [9]. Yet, surfactants can better prevent SeNP aggregation than these substances, as the former generally adsorb onto the NP surface through Coulomb or hydrophobic interactions during the NP assembly, controlling their size, morphology, and stabilization in suspension [2]. In this regard, surfactants are extensively employed for metal and metal oxide NPs; nevertheless, only a few studies report on similar strategies for SeNPs [2,10–18]. Furthermore, the latter involves mostly toxic and unsafe surfactants alongside energy-demanding and dangerous operational conditions, making it imperative to find feasible, inexpensive, bio- and eco-compatible strategies for SeNP production.

This study focuses on designing a novel, safe, cost-effective, and efficient confined environment for SeNP synthesis, unravelling the intricacies of this process and its effect on NP size, morphology, and stability, and bridging some theoretical foundations with experimental outcomes. Specifically, we chose the water-soluble, highly biocompatible, and unsaturated C_{18} sodium oleate (NaOl) as a surfactant for our confined environments and the essential amino acid L-cysteine (C) as a safe and effective SeO_3^{2-} reducing agent. By leveraging the synergistic effects of these two elements, we easily and rapidly generated high-quality, spherical, and stable SeNPs, overcoming issues related to pH conditions and precursor concentrations. Moreover, we studied the unique features of the L-cysteine@sodium oleate (C@NaOl) confined environments, showcasing its modulability for vesicle amount and size, which, in turn, strongly affect SeNP production, and delved into the intricate interplay of electrostatic and steric contributions governing SeNP stability over time. Lastly, we developed and introduced an innovative and efficient method for determining SeNP size by extending Mie's scattering theory of metal NPs to metalloid ones, providing a reliable and fast alternative to conventional size determination techniques, such as dynamic light scattering (DLS) analysis, Tauc-plot method, or electron microscopy (EM). Indeed, although these approaches are routinely used for NP size evaluation, they have significant limitations. DLS reliably estimates the NP size only if (i) these nanomaterials are spherical and monodisperse and (ii) their stabilizing agents do not self-assemble in the nanorange and take up a broad space. The Tauc-plot method highly depends on the intrinsic features and optical properties of NPs and their constitutive elements, whereas EM requires sample preparation and is time-demanding and expensive. Our method overcomes these issues and proves particularly effective for SeNPs from 40 to 100 nm in size, a dimensional range typical for most NPs obtained through reduction processes.

2. Materials and methods

2.1. Materials

Oleic acid (technical grade, 90 %, 364525), sodium hydroxide (NaOH, reagent grade, ≥98 %, pellets, anhydrous, S5881), L-cysteine (≥97 %, FG, W326205), sodium selenite (Na_2SeO_3, ≥90.0 % RT, anhydrous, 71950), sodium phosphate monobasic dihydrate ($NaH_2PO_4 \cdot 2H_2O$, essential grade, 98–100.5 % - calculated to the dried substance, 04269), sodium phosphate dibasic (Na_2HPO_4, BioXtra, ≥99 %, S7907), sodium carbonate ($NaHCO_3$, ACS reagent, ≥99.5 %, anhydrous, 222321), and sodium bicarbonate (Na_2CO_3, ACS reagent, ≥99.7 %, S6014) used in this study were purchased from Sigma Aldrich® (Milan, Italy). Carbon-coated copper grids (CF-300 CU), spectrophotometric acrylic and quartz cuvettes (pathlength 10 mm), and folded capillary Zeta cells were purchased from Electron Microscopy Sciences (PA, USA), Sarstedt (Milan, Italy), Hellma® (Milan, Italy), and Malvern Instruments (Milan, Italy), respectively.

2.2. Methods

2.2.1. Preparation of sodium oleate micelle solutions and C@NaOl dispersions

NaOl micelle solutions were prepared by adding an appropriate amount of sodium hydroxide solutions to oleic acid to obtain equimolar amounts of fatty acid and NaOH (16, 39, and 78 mM; final volume of 30 ml). NaOl concentrations were chosen to explore the effect of L-cysteine on the surfactant aggregates upon amino acid large excess (16 mM NaOl), defect (78 mM NaOl), or in intermediate conditions (39 mM NaOl). After titration, the suspensions were vortexed for 30 s and incubated at 25 °C for 3h to allow the formation of stable NaOl micelle solutions.

C@NaOl dispersions were obtained by dissolving appropriate amounts of L-cysteine into the NaOl solutions to reach the desired final concentrations of 18, 24, 36, or 72 mM of amino acid, except for monitoring pH and conductivity variations. In the latter cases, 200 mM stock dispersions of L-cysteine in 16, 39, or 78 mM NaOl were prepared and used to titrate equimolar surfactant solutions.

2.2.2. Physical-chemical characterization of NaOl solutions and C@NaOl dispersions

The obtained NaOl and C@NaOl dispersions were characterized through UV–Visible spectroscopy, pH evaluation, conductivity measurements, DLS and ζ potential analyses, and ATR-FTIR spectroscopy. Absorption spectra of aliquots (20 μl diluted in 2 ml of distilled water) of NaOl solutions and their C_{72}@NaOl counterparts (where 72 refers to 72 mM L-cysteine) were recorded in the 200–800 nm range through a Beckman DU 800 spectrophotometer (Beckman Coulter Life Sciences).

pH and κ values were determined for NaOl solutions and C@NaOl dispersions increasing L-cysteine content by titrating NaOl solutions with the appropriate amount of the stock C@NaOl dispersions mentioned in the previous paragraph through a pH 211 microprocessor pH meter (Hanna Instruments) and 160 conductivitymeter (Amel Instruments).

DLS and ζ potential measurements were performed on 1 ml aliquots of NaOl solutions and their corresponding C@NaOl dispersions containing 18, 24, 36, or 72 mM amino acid (100 scans per replicate, acquisition time 30 s) under isothermal conditions (T = 25 °C) through a Zen 3600 Zetasizer Nano ZS (Malvern Instruments) [19].

ATR-FTIR spectra were collected for NaOl solutions and C@NaOl dispersions containing 72 mM L-cysteine through a Bruker Vertex70 Advanced Research FTIR spectrometer (Bruker Instruments) equipped with a platinum ATR and a diamond (η = 2.4) crystal. Spectra were acquired in the 4000-600 cm^{-1} range (2 cm^{-1} lateral resolution, 200 scans) and analysed through OPUS7.5 (Bruker Instruments) and Origin 2016 software. Spectral deconvolutions by nonlinear least-square fitting were performed using Origin 2016 software, and peak integrals of interest were duly normalized for further analysis against integrals calculated in the 1800-1200 cm^{-1} region [20].

2.2.3. Synthesis of SeNPs in the aqueous environment and their characterization

SeNPs were synthesized in water using the known redox reaction between SeO_3^{2-} and SH-containing compounds [21], in our case

L-cysteine. Briefly, SeNPs were produced using a 1:3, 1:4, or 1:6 M ratio of Na_2SeO_3 (100 mM stock solution) and L-cysteine (100 mM stock solution) using water as solvent. The same ratios were used to generate SeNPs in buffered neutral or alkaline environments using phosphate (1 M NaH_2PO_4 and 0.63 M Na_2HPO_4, pH = 7.0) and carbonate (0.013 M $NaHCO_3$ and 0.087 M Na_2CO_3, pH = 9.0) buffers as solvents.

The as-obtained SeNPs were characterized through UV–Visible and ATR-FTIR spectroscopies, DLS and surface charge measurements, as mentioned above. Kinetics of SeNP formation in water or buffered conditions was monitored by collecting UV–Visible spectra of NP dispersions after 1, 5, 10, and 30 min from the synthesis. Moreover, the size and morphology of these SeNPs were evaluated through Scanning Electron Microscopy (SEM) using a FEG-SEM FEI versa 3D™ microscope (Thermo Fischer Scientific Electron Microscopy Solutions) at an accelerating voltage of 10 kV. For SEM imaging, 5 μl aliquots of SeNP dispersions were deposited onto carbon-coated copper grids and air-dried. The size distribution and average diameter of SeNPs were obtained by measuring 100 randomly chosen NPs using ImageJ software [20].

2.2.4. Synthesis of SeNPs in confined environments and their characterization

SeNP synthesis in confined environments (SeNPs@NaOl) was performed by adding Na_2SeO_3 (100 mM stock solution in water) aliquots (6 mM final concentration) to C@NaOl dispersions to maintain 1:3, 1:4, and 1:6 ratio between SeO_3^{2-} and L-cysteine (18, 24, or 36 mM final concentration). SeNPs@NaOl were also obtained by improving up to 3-fold SeO_3^{2-} and L-cysteine concentrations (18 and 72 mM, respectively) to study the stability of these NPs and increase their production yield.

SeNPs@NaOl were characterized following the same methods described for those obtained in water, except for EM imaging, which was performed using the same microscope in scanning transmission mode (STEM), alongside X-ray photoelectron (XPS) and Raman spectroscopies. XPS was performed through a PHI5000 VersaProbe II Scanning XPS Microprobe (ULVAC-PHI) working with an Al anode (Al K_α = 1486.6 eV), focusing the beam to a diameter of 200 μm (50 W) using both positive (Ar^+) and negative (e^-) charge neutralization and a 45° electron take-off angle. High-resolution spectra (0.1 eV) for the C1s and Se3d regions were collected. The XPSPEAK v4.0 software was used to correct binding energies using the C1s aliphatic carbon peak (284.8 eV) as internal standard and to analyse the obtained spectra utilizing a nonlinear least-square fitting procedure to resolve chemically different C and Se species. Raman spectra were acquired with a Horiba Raman spectrometer (HORIBA Scientific) using a 633 nm excitation laser (1 % laser power – ND filter –, acquisition time: 16 s, number of independent runs: 5) in the 10-550 cm^{-1} range. Deconvolutions of Raman spectra by nonlinear least-square fitting using Lorentzian curves were performed through Origin 2016 software in the 230-280 cm^{-1} region. For both XPS and Raman measurements, aliquots (10 μl) of SeNP dispersions were drop casted onto an aluminium foil and air dried over night at room temperature. Besides, SeNPs@NaOl stability was monitored through UV–Visible spectroscopy after 0, 8, 24, 32, 48, 56, 72, 96, and 120h from their synthesis at room temperature.

2.2.5. Determination of SeNP size

The size of SeNPs obtained in water or C@NaOl confined environments was firstly assessed through commonly used techniques and models, i.e., DLS measurements and the Tauc-plot method; the latter is extensively described in the Supplementary File, section 3.2.1. Given the inaccuracies of these methods in establishing SeNP size, we developed and implemented an innovative and reliable model based on Mie's scattering theory and UV–Visible spectroscopy, whose details are reported in the Supplementary File, section 3.2.3.

2.2.6. Statistical analysis

Experiments and spectral deconvolutions were performed in triplicate ($n = 3$) and, when pertinent, results are reported as average values with standard deviation.

The obtained data underwent a one-way ANOVA analysis using Origin 2016 software and the statistical significance of these results was assessed through the Tukey's Honestly Significant Difference (HSD) test. Results were considered statistically significant when $p < 0.05$.

3. Results

3.1. The L-cysteine@NaOl (C@NaOl) confined environment

C@NaOl confined environments were studied by focusing on different surfactant and amino acid concentrations and their interactions (Fig. 1). Confined environments are henceforth indicated as C_X@$NaOl_Y$, where X and Y represent the L-cysteine and NaOl concentrations used to obtain such dispersions; the C@$NaOl_Y$ acronym refers to confined environments at a fixed surfactant and variable amino acid concentrations.

NaOl dispersions exhibited UV absorbance at ca. 230 nm originating from the surfactant C=C chromophore group (Fig. 1a). Besides, a secondary absorbance peak at ca. 280 nm emerged in $NaOl_{39}$ and $NaOl_{78}$, albeit with lower intensity. Irrespective of surfactant concentration, colloids featured pH > 10.6 and high κ values ranging from 1.16 ($NaOl_{16}$) to 3.9 mS cm^{-1} ($NaOl_{78}$) (Fig. 1c and d). This evidence, alongside DLS measurements, indicates the surfactant self-assembly in polydisperse (PdI >0.5) spherical and/or ellipsoidal micelles (L_1 phase) with comparable hydrodynamic diameters (d_H) of ca. 30 nm (Fig. 1 c-e; Table S1). Colloidal dispersions showed highly negative surface potentials (Fig. 1f) deriving from the dissociated surfactant $-COO^-$ head groups. Except for d_H, these parameters depended on the NaOl concentration, governing surfactant aggregate behaviour.

Introducing L-cysteine made dispersions cloudy with broader UV–Visible spectra, although the absorbance peak at 230 nm remained visible (Fig. 1b). The amino acid lowered the pH of dispersions, ranging from 7.7 (C_{100}@$NaOl_{16}$) to 10.0 (C_{10}@$NaOl_{78}$), depending on NaOl and L-cysteine concentrations (Fig. 1c). Within this pH interval, NaOl self-assembled into a mixture of micelles and vesicles, the latter identified as the $L_{\alpha L}$ phase [22,23]. Conductivity, DLS, and ζ potential measurements supported this hypothesis. Indeed, even low L-cysteine concentrations significantly decreased the dispersions' conductivity (Fig. 1d), indicating vesicle formation [24,25]. The extent of this phenomenon correlated with the NaOl:L-cysteine ratio, with the most pronounced drop when introducing 5 (Δκ = 0.42 mS cm^{-1}), 10 (Δκ = 0.36 mS cm^{-1}), or 16 (Δκ = 1.00 mS cm^{-1}) mM L-cysteine to 16, 39, or 78 mM NaOl, respectively. κ improved with increasing L-cysteine concentration, suggesting vesicle enlargement [20]. Yet, constant κ values and, hence, vesicle stability [26] were detected within the 9–18 mM and 13–40 mM L-cysteine range for C@$NaOl_{39}$ and C@$NaOl_{78}$, respectively. DLS measurements confirmed vesicle stability, showing comparable d_H values of ca. 50 nm for C@$NaOl_{39}$ and C@$NaOl_{78}$ dispersions at the mentioned L-cysteine concentrations (Fig. 1e). Large vesicles (>200 nm) were produced when [L-cysteine]>[NaOl], aligning with conductivity curves. ζ potential measurements revealed trends comparable to conductivity for C@$NaOl_{39}$ and C@$NaOl_{78}$, while C@$NaOl_{16}$ showed values that monotonically rose with increasing amino acid concentration (Fig. 1f).

Surfactant-amino acid interactions and modifications were elucidated through ATR-FTIR spectroscopy (Fig. 2; Table S2). NaOl dispersions featured IR signals related to surfactant functional groups, with intense contributions from $-CH_2$ and $-CH_3$ alkyl chain (2960-2850 cm^{-1}) and the $-COO^-$ (1558 cm^{-1}) stretching vibrations [27]. Vibrational modes of water varied with NaOl concentration, with $NaOl_{16}$ lacking $-OH$ stretching (3400-3200 cm^{-1}) and bending (ca. 1650 cm^{-1}) vibrations, suggesting its limited interaction with water molecules.

The hydrogen bond network further varied upon adding L-cysteine to NaOl. L-cysteine also determined the disappearance of the surfactant asymmetric $-CH_3$, $-CH$, symmetric $-COO^-$, and $-CO$ stretching and $-CH_2$ *trans* bending vibrations, the shift of the $-CC$ stretching and $-CH_2$ (closed
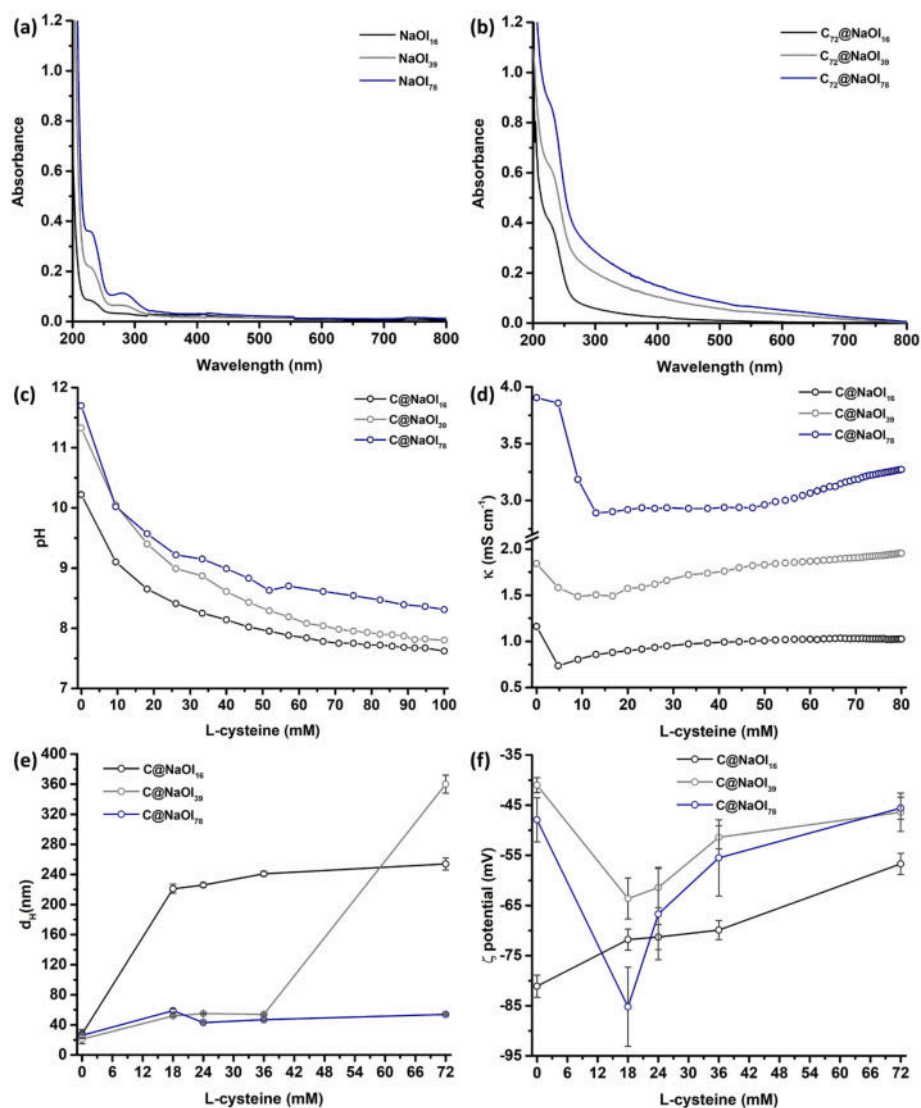
Fig. 1. Physical-chemical characterization of NaOl and C@NaOl colloidal dispersions. (**a,b**) UV–Visible spectra, (**c**) pH evaluation, (**d**) conductivity (κ), (**e**) hydrodynamic diameter (d_H), and (**f**) zeta (ζ) potential of surfactant dispersions obtained by using 16, 39, or 78 mM NaOl – indicated as $NaOl_{16}$, $NaOl_{39}$, or $NaOl_{78}$ - and varying L-cysteine concentrations. In (**b**) L-cysteine concentration is 72 mM – indicated as C_{72}. Results represented in panels (**e-f**) for C@NaOl dispersions obtained using different surfactant concentrations underwent a one-way ANOVA analysis and the subsequent Tukey's Honestly Significant Difference (HSD) test; (**e**) d_H values were statistically different ($p < 0.05$) under all conditions, whereas no statistical significance ($p > 0.05$) was detected between (**f**) ζ potential values of $C@NaOl_{39}$ and $C@NaOl_{78}$ dispersions.

to the NaOl unsaturation) bending peaks towards higher wavenumbers, and variations in bending and symmetric stretching vibrations deriving from the amino acid $-NH_3^+$ groups. These changes depended on NaOl:L-cysteine ratios, with $C_{72}@NaOl_{78}$ showing the most variable spectrum. When [L-cysteine]>[NaOl], vibrations related to the surfactant HC=CH group and $-NH_3^+$, $-CN$, and $-NH_2$ groups and $O\cdots H^+$-O overtone of L-cysteine varied in position and presence/absence. The intermediate scenario – i.e., $C_{72}@NaOl_{39}$ – revealed also significant changes pertaining to the peak position and loss of $-NH_3^+$ stretching and rocking vibrational modes. In $C_{72}@NaOl_{78}$, several IR signals related to L-cysteine (-NH_2, $-NH_3^+$, $-CH_2$, CN) or NaOl (-COO-, $-CO$, trans $-CH_2$, and HC=CH) either shifted or disappeared, and, simultaneously, new peaks, referring to stretching and bending vibrations of L-cysteine protonated amino groups arose. Specifically, the peak centred at 1260 cm^{-1} likely correlated with the $-CH_2$ twisting mode under alkaline conditions [28], aligning with pH evaluation (Fig. 1d), whereas the new peak at 1620 cm^{-1} derives from the deformation of $-NH_3^+$. The latter, alongside the shift of the symmetric $-NH_3^+$ bending (from 1510 to 1514 cm^{-1}) and the

NaOl asymmetric -COO- stretching (from 1558 to 1562 cm^{-1}) vibrations, suggested the occurrence of salt bridging between NaOl and L-cysteine. Spectral deconvolutions in the 1700-1520 and 1460-1300 cm^{-1} regions confirmed this indication, as all $C_{72}@NaOl$ dispersions displayed IR absorbance in the 1610-1620 cm^{-1} range typically attributed to $-NH_3^+$ deformation modes (Figs. S1 and S2; Table S3). Moreover, $C_{72}@NaOl_{78}$ dispersion showed contributions typical of free NaOl molecules, significant variation for CH_2 bending and rocking vibrations, and disappearance of several $-NH_3^+$ bending and -COO- stretching vibrations of L-cysteine not detected for other colloids.

Regardless of the modifications exerted by L-cysteine on the NaOl aggregates, ATR-FTIR spectra of C@NaOl dispersions showed $-SH$ stretching vibrations (ca. 2540 cm^{-1}), indicating the availability of this group for reducing SeO_3^{2-} to Se^0.

3.2. Synthesis of selenium nanoparticles

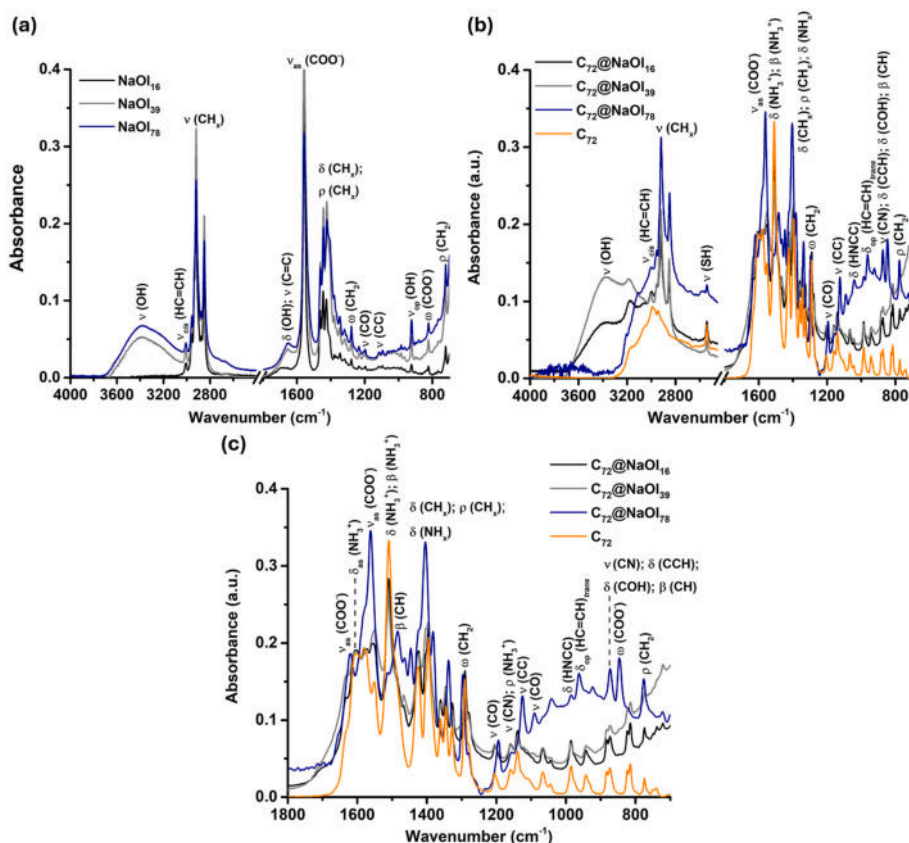Complete oxyanion reduction necessitates a 1:4 M ratio between

Fig. 2. ATR-FTIR spectra of NaOl and C@NaOl dispersions. Panel (**a**) reports spectra of NaOl colloids at different concentrations, whereas in (**b**) spectra of L-cysteine aqueous solution and C@NaOl dispersions are displayed. Panel (**c**) shows an enlargement of spectra referring to (**b**) in the 1800-700 cm^{-1} region. In (**b,c**), L-cysteine concentration is 72 mM either in aqueous solution or in NaOl dispersions.

SeO_3^{2-} and SH-containing substances [21]. To investigate the impact of the confined environment on SeNP production, we explored this ratio (SeO_3^{2-} initial concentration = 6 mM), a deficiency (1:3), and an excess (1:6) of L-cysteine. Furthermore, since SeNPs generated in water instantaneously form insoluble Se crystals when SeO_3^{2-} > 6 mM, we examined whether C@NaOl dispersions may enhance NP yield using an 18 mM (SeO_3^{2-}): 72 mM (L-cysteine) ratio, henceforth indicated as 1:4H. Initially, SeNP synthesis in water employed the same SeO_3^{2-}:L-cysteine ratios for subsequent comparative analysis.

3.2.1. SeNPs in the aqueous environment

Aqueous suspensions containing SeO_3^{2-} and L-cysteine exhibited a distinct red colouration (Fig. 3 a) typical of Se^0. Similar to metal NPs, exciton resonance or transition occur when irradiating SeNPs [7], thus UV–Visible spectroscopy can monitor their formation. SeNPs displayed broad absorbance extending up to 550 nm, whose width and intensity depended on the chosen precursor ratio (Fig. 3c). SeNPs 1:3 exhibited the lowest absorbance, attributed to the incomplete SeO_3^{2-} reduction. Moreover, SeNPs 1:3 and 1:4 featured an absorbance peak at ca. 253 nm, blueshifting to 232 nm for SeNPs 1:6, and a pronounced absorbance
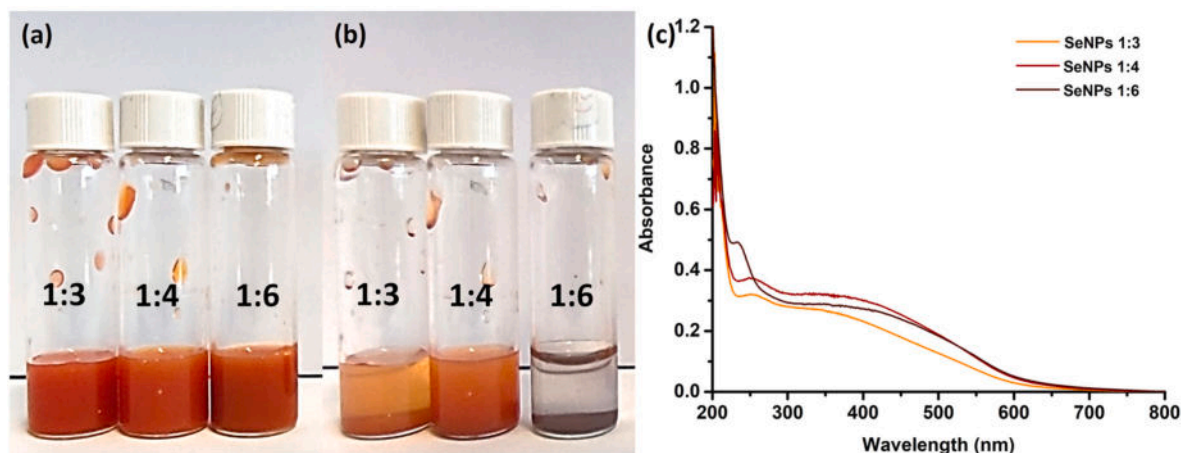

Fig. 3. SeNPs produced in the aqueous environment. (**a**) SeNP colloids after the synthesis and (**b**) incubated at room temperature for 24h, where NP precipitation and aggregation in grey crystals is visible. Panel (**c**) shows UV–Visible spectra collected for SeNPs 1:3, 1:4, and 1:6.

shoulder. SeNPs 1:4 and 1:6 exhibited wider absorbance than SeNPs 1:3, indicating, alongside the intensity variation among the former, different NP morphology and size [7,21]. Indeed, although this process yielded spherical SeNPs under all conditions, non-regular Se nano or micro aggregates were observed when L-cysteine was in excess (Fig. 4 a-c). The oxyanion-to-reducing agent ratio influenced SeNP size, which was 54 ± 16 nm, 103 ± 18 nm, and 121 ± 20 nm upon using a 1:3, 1:4, and 1:6 precursors ratio, respectively. Moreover, SeNPs were polydisperse and unstable, particularly SeNPs 1:6, aggregating and precipitating within 24-h (Fig. 3 b; Fig. S3).

Although the available literature suggests that the weak stabilization of SeNPs in water derives from electrostatic interactions solely mediated by cystine (RSSR) molecules, ATR-FTIR spectroscopy (Fig. S4; Tables S4–S5) was performed to identify other species potentially contributing to this phenomenon. The obtained spectra reveal vibrational modes that, based on our previous Density Functional Theory (DFT) calculations [29], are attributed to RSSR, cysteine sulfinic (RSO_2^-), and cystine monoxides (RSOSR), either as residues or adsorbed onto the SeNP surface, alongside L-cysteine excess for SeNPs 1:6.

Considering the alkaline nature of C@NaOl confined environments, SeNP synthesis in water was monitored through UV–visible spectroscopy at pH 7.0 and 9.0 to explore potential changes in the reaction rate, NP size, and morphology. Kinetics profiles revealed that SeNPs were immediately formed in the unbuffered suspensions (pH = ca. 5.0) and did not underwent changes within 30 min timeframe (Figs. S5a,d,g). In contrast, a neutral or basic pH influenced both the absorbance intensity and broadness (Figs. S5b,c,e,f,h,i), indicating variations in NP rate of formation, size, and morphology. At pH 9.0, a delayed NP generation and a shift in the principal absorbance peak were observed up to 5–10

min, while absorbance broadening up to 650 nm was typical for both buffered systems. The correlation between the latter phenomenon and variation in NP size and shape was proved by SEM imaging, which showed bigger NPs, micro aggregates, and Se crystals in buffered suspensions regardless of the precursor ratio used (Fig. 4d–i).

3.2.2. SeNPs in C@NaOl confined environments

C@NaOl confined environments efficiently facilitate SeNP formation, as, regardless of the NaOl concentration or the SeO_3^{2-}:L-cysteine ratio, vibrant red suspensions were successfully obtained under all experimental conditions (Fig. 5a–d). Consistent with UV–Visible spectra of SeNPs in water, those obtained in C@NaOl dispersions featured a distinct absorbance peak at ca. 250 nm (Fig. 5e–g,h). Yet, confined environments increased the peak resolution and restricted the absorbance to 500 nm, suggesting that SeNPs@NaOl are smaller and less polydisperse than in the aqueous system. No colour changes or NP precipitation was macroscopically detected when using the C@NaOl dispersions (Fig. 5a–c), showing their strength in stabilizing SeNPs. Furthermore, SeNPs@NaOl$_{39}$ and SeNPs@NaOl$_{78}$ displayed a third absorbance contribution in the 200–215 nm range, likely attributable to NPs<50 nm [7]. Even increasing the precursor concentrations up to 18 mM SeO_3^{2-} and 72 mM L-cysteine (i.e., 1:4H) yielded similar results (Fig. 5), which hold significant implications for technological purposes, avoiding the instantaneous SeNP aggregation into black precipitates observed in water.

SeNP@NaOl formation was more comprehensively investigated by closely monitoring its short-term kinetics (1–30 min) (Fig. S6).SeNPs formed instantly under alkaline conditions (7.9 < pH < 9.7) when using C@NaOl dispersions, highlighting the importance of the surfactant in
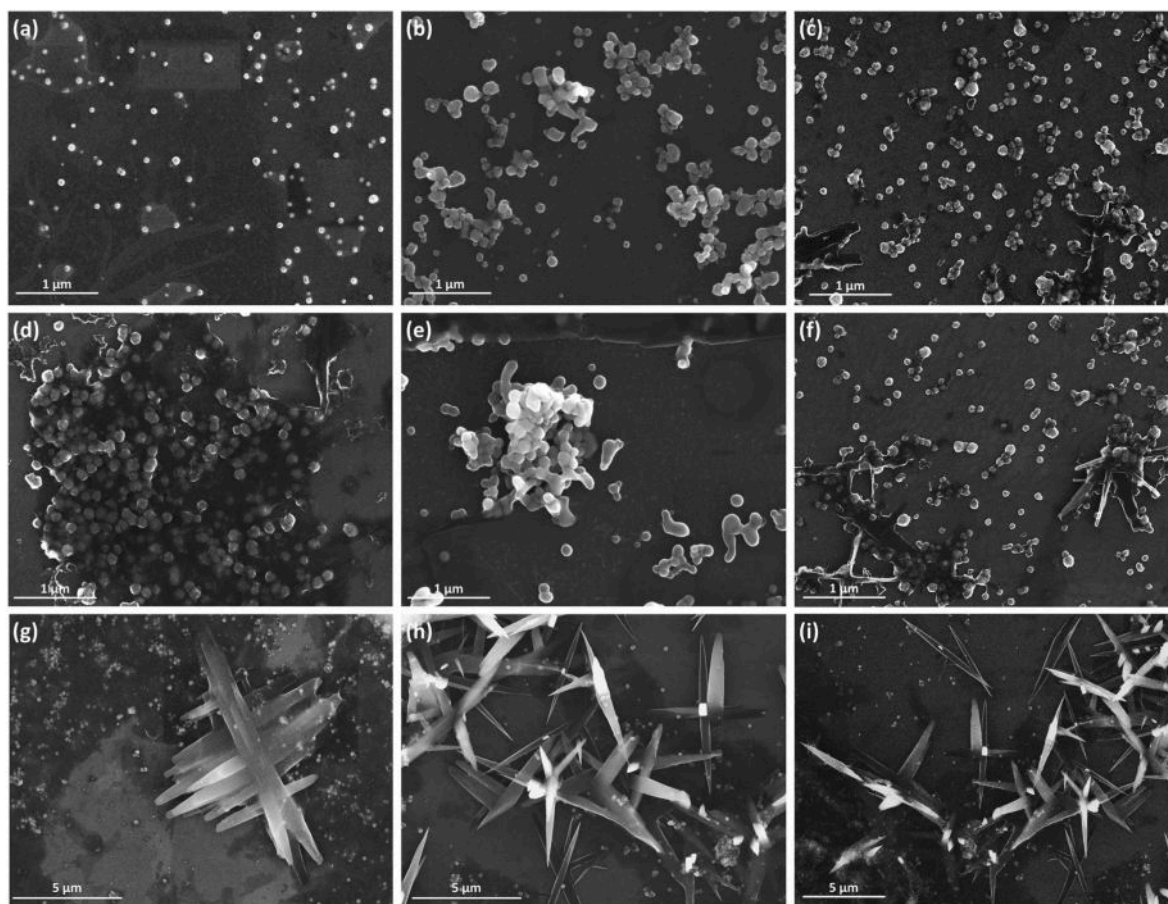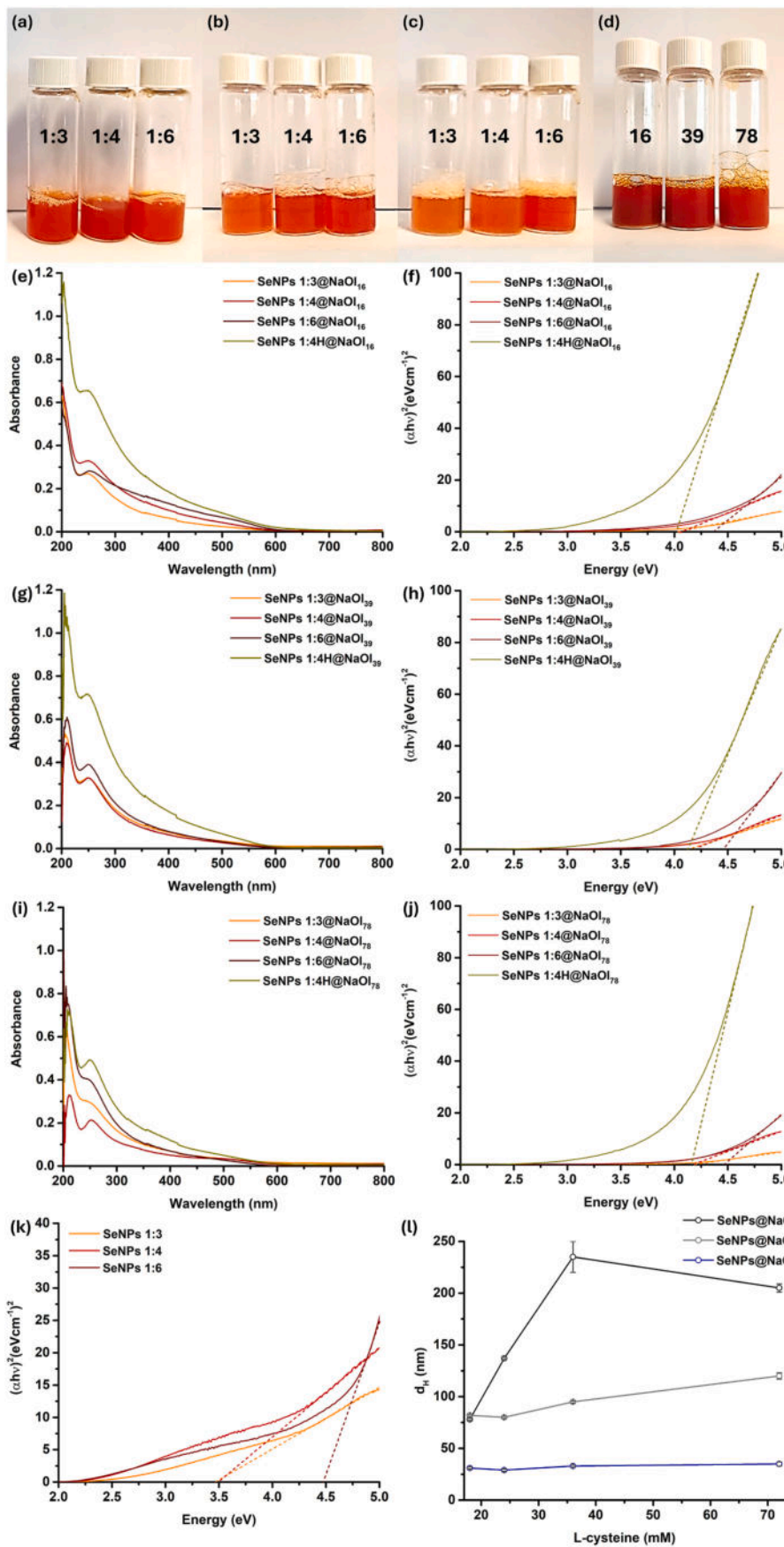

Fig. 4. Scanning Electron Microscopy (SEM) images of SeNPs produced in the aqueous environment. SeNPs obtained using a (**a,d,g**) 1:3, (**b,e,h**) 1:4, and (**c,f,i**) 1:6 ratio between Na$_2$SeO$_3$ and L-cysteine at (**a-c**) uncontrolled pH (ca. 5.0), (**d-f**) pH = 7.0, or (**g-i**) pH = 9.0.

Fig. 5. SeNPs@NaOl dispersions and their optical properties. (**a-c**) Images of SeNPs@NaOl dispersions after 30 min from the synthesis using 1:3, 1:4, or 1:6 ratios between Na_2SeO_3 and L-cysteine in the C@NaOl confined environment and (**a**) 16, (**b**) 39, or (**c**) 78 mM NaOl. Panel (**d**) displays SeNPs@NaOl dispersions obtained by using 1:4H (18 mM:72 mM) ratio between Na_2SeO_3 and L-cysteine and 16, 39, or 78 mM NaOl. The optical properties of SeNPs@NaOl were determined through (**e,g,i**) UV–Visible spectra, and their corresponding (**f,h,j**) Tauc plot were obtained and used to estimate SeNP size. The same procedure was also used for SeNPs in water, whose Tauc plot is reported in panel (**k**). An indication of SeNPs size was obtained through DLS measurements by determining (**l**) d_H values of these dispersions, which are statistically different ($p < 0.05$) as a function of the NaOl concentration used for SeNP synthesis, as highlighted by the one-way ANOVA analysis and the subsequent Tukey's Honestly Significant Difference (HSD) test.

governing the rate of NP formation. When [L-cysteine]<[NaOl], UV–Visible spectra revealed a slower rate of SeNP formation than upon L-cysteine excess, as indicated by the increased absorbance over 30 min particularly noticeable for NaOl$_{39}$ (Figs. S6e–h).

3.2.2.1. Estimation of SeNP size using conventional models and approaches. We initially estimated the size of SeNPs using conventional methods, namely the Tauc plot model and DLS measurements (Fig. 5f–h, j,k).

Tauc plots and band gap (E_g) values for SeNPs@NaOl were obtained from UV–Visible spectra (SI, section 3.2.2). E_g values ranged between 3.98 and 4.42 eV (Table S6), surpassing bulk Se ($E_g = 1.6$–2.1 eV). According to the relationship between E_g and the NP size, SeNPs@NaOl should all feature comparable diameters smaller than 2 nm (Table S6), regardless of the synthesis conditions. However, this result seems impractical, as reduction methods typically yield SeNPs ranging in size between 20 and 200 nm [6]. To assess the validity of this method for SeNPs, NP water dispersions underwent the same analytical procedure (Fig. 5k), revealing lower E_g values for SeNPs 1:3 and 1:4 than the SeNP@NaOl counterparts; in contrast, SeNPs 1:6 featured a E_g value of ca. 4.42 eV. Even for water SeNP dispersions, the size estimation following this model was inaccurate, as it predicts 1.59–2.09 nm diameter NPs, contrary to previous studies [7,17,18] and SEM imaging (Fig. 4a–c).

d_H values obtained from DLS measurements for SeNPs@NaOl showed similar trends to C@NaOl dispersions (Fig. 5l; Tables S1 and S7), and they were affected by the NaOl:L-cysteine ratio and SeO_3^{2-} concentration used. Since SeO_3^{2-} always fell short of other components, d_H values generally reflected the corresponding confined environments. Only SeNPs 1:3@NaOl$_{16}$ featured d_H (ca. 78 nm) sensibly different than its C_{18}NaOl$_{16}$ counterpart (ca. 221 nm), likely due to the low surfactant and amino acid concentration used. Moreover, these dispersions contained differently sized aggregates (SeNPs, NaOl vesicles and/or micelles, and cystine crystals) that hindered the NP size determination and contributed to their overall polydispersity (PdI >0.30). Similar results were obtained even for SeNPs produced in water, likely due to cystine crystals and L-cysteine in excess, revealing d_H bigger than the actual SeNP diameter determined through SEM imaging.

3.2.2.2. A new model based on UV–visible spectroscopy and Mie's scattering theory for evaluating SeNP size. Mie's scattering theory is a useful approach for determining the NP size and shape based on its extinction of an incident beam. This approach is routinely used for Ag and Au NPs, which feature significant SPR bands in the visible range. However, this theory has not been extended to date to SeNPs, as they do not display SPR phenomena per sè. Yet, since Se confined in the nanorange manifest exciton resonance or transition phenomenologically comparable to metal SPR [7], Mie's scattering theory for metal NPs was here applied to SeNPs, and their UV–Visible contributions were used to implement an innovative model for evaluating their size (SI, section 3.2.3).

As for metal NPs, UV–Visible spectra simulations for differently sized SeNPs showed variation in peak position and width depending on their size (Fig. S7a). A linear relationship ($R^2 = 0.989$) between the absorption wavelength (λ_{abs}) and SeNP diameter (50–120 nm range) was observed (Fig. S7b). Given the broadness of SeNPs@NaOl UV–Visible spectra, they underwent deconvolution in the 200–700 nm region, always revealing multiple contributions, hence SeNP populations, with

different positions and areas depending on the C@NaOl concentration and Na_2SeO_3-to-L-cysteine ratio used (Fig. S8; Table S8). Only dispersions obtained using 16 mM NaOl featured four contributions, whereas increasing the surfactant concentration led to five populations. From spectral deconvolutions, the SeNP size was determined as described in section 3.2.3; results from the model are depicted in Fig. 6. Under all synthetic conditions, most SeNPs seemed to be smaller than 70 nm, suggesting the ability of C@NaOl confined environments to limit their growth regardless of the Na_2SeO_3-to-L-cysteine ratio used. Increasing the surfactant concentration progressively reduced the SeNP size, whose most represented population shifted from 56-70 nm to 40–55 nm when using 16 or 78 mM NaOl, respectively. Yet, the same component negatively influenced the SeNP polydispersity, as inferred by the high number of NP populations observed upon adding 39 or 78 mM NaOl, displaying 3 or 4 NP contributions, respectively. Moreover, only C@NaOl$_{78}$ dispersions seemed to mediate the formation of SeNPs with an average size in the 71–85 nm range.

3.2.2.3. Validation of the SeNP size estimation by Scanning Electron Microscopy in transmission (STEM) mode. STEM imaging of SeNPs 1:4@NaOl confirmed the production of spherical SeNPs (Fig. 7), corroborating the validity of UV–Visible spectral simulations based on this nanomorphology. These SeNPs were also embedded in a slightly electron-dense material constituted by NaOl. The latter was either organized as elongated aggregates at high surfactant concentrations or present as less defined structures, almost wrapping and confining SeNPs, when using 16 mM NaOl, suggesting that low surfactant amount can better stabilize SeNPs. STEM size distributions confirmed this observation, as SeNPs 1:4@NaOl$_{16}$ were less polydisperse than other samples (Fig. 8a). Furthermore, SeNPs 1:4@NaOl featured size distributions like those observed when using other cationic or anionic surfactants as confined environments [2,10,15,16]. More importantly, STEM images corroborated the validity of the implemented model for SeNP diameter evaluation, as the two size distributions significantly overlapped for NPs between 40 and 100 nm under all experimental conditions (Fig. 8).

3.2.2.4. SeNP stability. SeNPs@NaOl dispersions were macroscopically stable for more than two months, as highlighted by the absence of precipitate in the vials (Fig. 9 a-d). This evidence was corroborated by SEM imaging, which showed that SeNPs retained the typical spherical shape after one month of storage at room temperature(Fig. S15). The stability of such dispersions was deeply investigated by monitoring the NP precipitation kinetics up to five days from the synthesis and applying the implemented model to evaluate NP variation in size over time. UV–Visible spectra of SeNPs@NaOl dispersions showed little modifications and limited NP precipitation (Figs. S9 and S10). Yet, the UV–Visible spectra broadness increased over the timeframe considered, being the largest after five days. Deconvolutions of UV–Visible spectra highlighted significant variations in integral values and absorbance contributions of SeNP@NaOl dispersions (Figs. S11–13; tables S9–S11). Specifically, 16 mM NaOl guaranteed to maintain two contributions at similar wavelengths within five days, although their integrals varied with time. The latter phenomenon was observed using the other NaOl concentrations, which also caused the disappearance of absorbance signals in the 205–245 nm and 275–305 nm (SeNPs@NaOl$_{78}$) range over five days, depending on the chosen surfactant amount and the Na_2SeO_3:L-cysteine ratio. Aligning with these observations, estimating the NP size
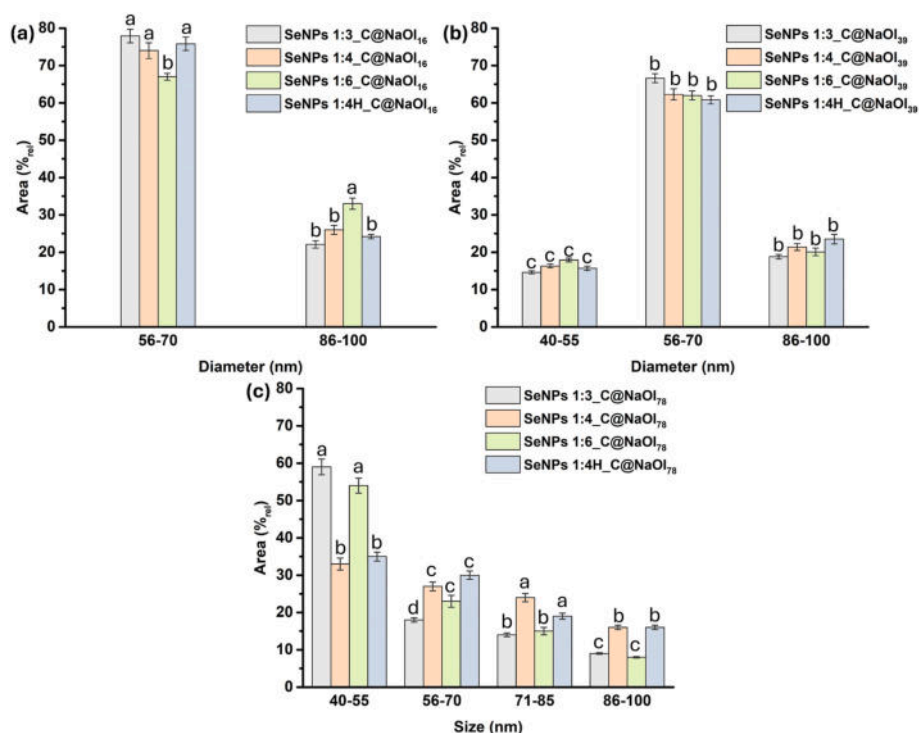
Fig. 6. Application of the developed model based on Mie's scattering theory for determining SeNPs size. Size distribution of SeNPs@NaOl produced by using (**a**) 16, (**b**) 39, or (**c**) 78 mM NaOl according to the implemented model. The statistical significance of normalize integrals referring to each SeNP population (i.e., 40–55, 56–70, 71–85, 86–100 nm; independent variables) within SeNPs@NaOl obtained using either 16, 39, or 78 mM NaOl was assessed through the one-way ANOVA analysis and the subsequent Tukey's Honestly Significant Difference (HSD) test. Different letters represent statistically different integrals ($p < 0.05$) from the largest value (*a*) to the smallest (*c, d, b,* and *c* for NPs of 40–55, 56–70, 71–85, and 86–100 nm) one.
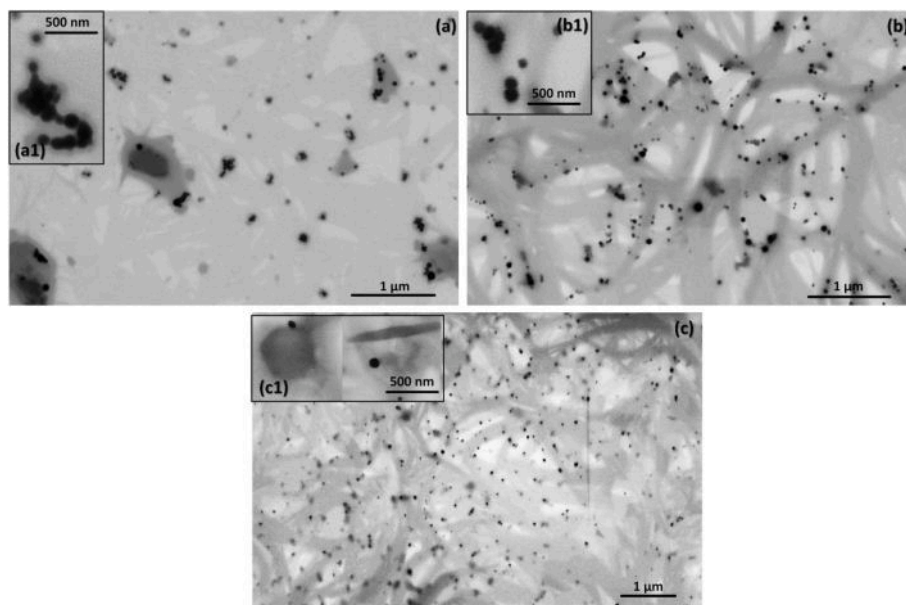

Fig. 7. Scanning Electron Micrographs in Transmission (STEM) mode of SeNPs produced in C@NaOl confined environments. STEM was performed on SeNPs synthesized by using (**a**) 16, (**b**) 39, or (**c**) 78 mM NaOl and the stoichiometric 1:4 ratio between Na_2SeO_3 and L-cysteine. Inlets (**a1-c1**) show higher-magnification images of the as-produced SeNPs.

through the developed model revealed a dynamic evolution of these dispersions. Nevertheless, most NPs (Area$_{rel}$ > 50 %) were between 56 and 70 nm in size over the five-day interval (Fig. 9e–g; Fig. S14). Indeed, although small SeNPs (d < 56 nm) were obtained with 39 or 78 mM NaOl, they were the most unstable. This phenomenon directly correlated to the C@NaOl confined environment used. When [NaOl]>[L-cysteine],

small SeNPs, alongside those between 71 and 85 nm within SeNPs@-NaOl$_{78}$, dissolved in 2–3 days, contributing to the rising of the 56–70 nm population. On the opposite, the [L-cysteine]≥[NaOl] scenario maintained only two SeNP populations in C@NaOl$_{16}$ dispersions and small NPs in SeNPs 1:4H@NaOl$_{39}$, which featured three stable NP populations (Fig. S14a-d,h). Nevertheless, integrals referring to large SeNPs (>80
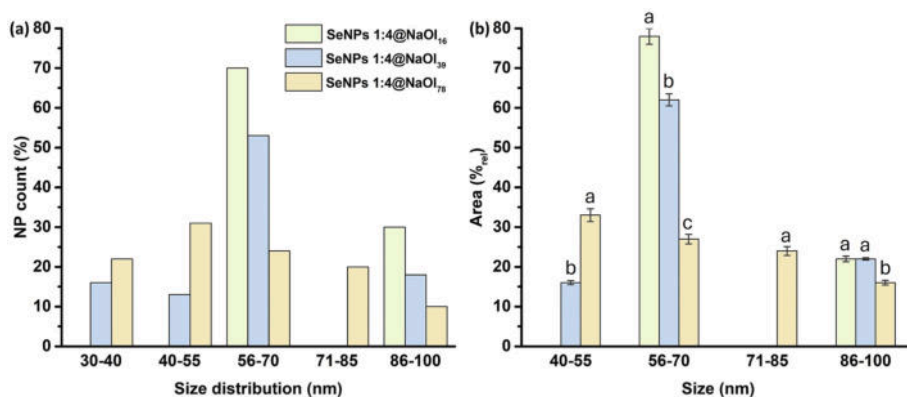
Fig. 8. Comparison between size distributions of SeNPs 1:4@NaOl. Size distribution obtained from (**a**) STEM images and (**b**) the implemented model for SeNP size evaluation. In panel (**b**), the statistical significance of normalize integrals referring to each NP 1:4 population (i.e., 40–55, 56–70, 71–85, 86–100 nm; independent variables) within SeNPs@NaOl obtained using either 16, 39, or 78 mM NaOl was assessed through the one-way ANOVA analysis and the subsequent Tukey's Honestly Significant Difference (HSD) test. All integrals related to the independent variables (i.e., size intervals) were statistically different ($p < 0.05$), as indicated by the diverse letters (*a* for the largest integral of each variable), exception for SeNPs of 86–100 nm within SeNPs 1:4@NaO$_{16}$ and SeNPs 1:4@NaOl$_{39}$.
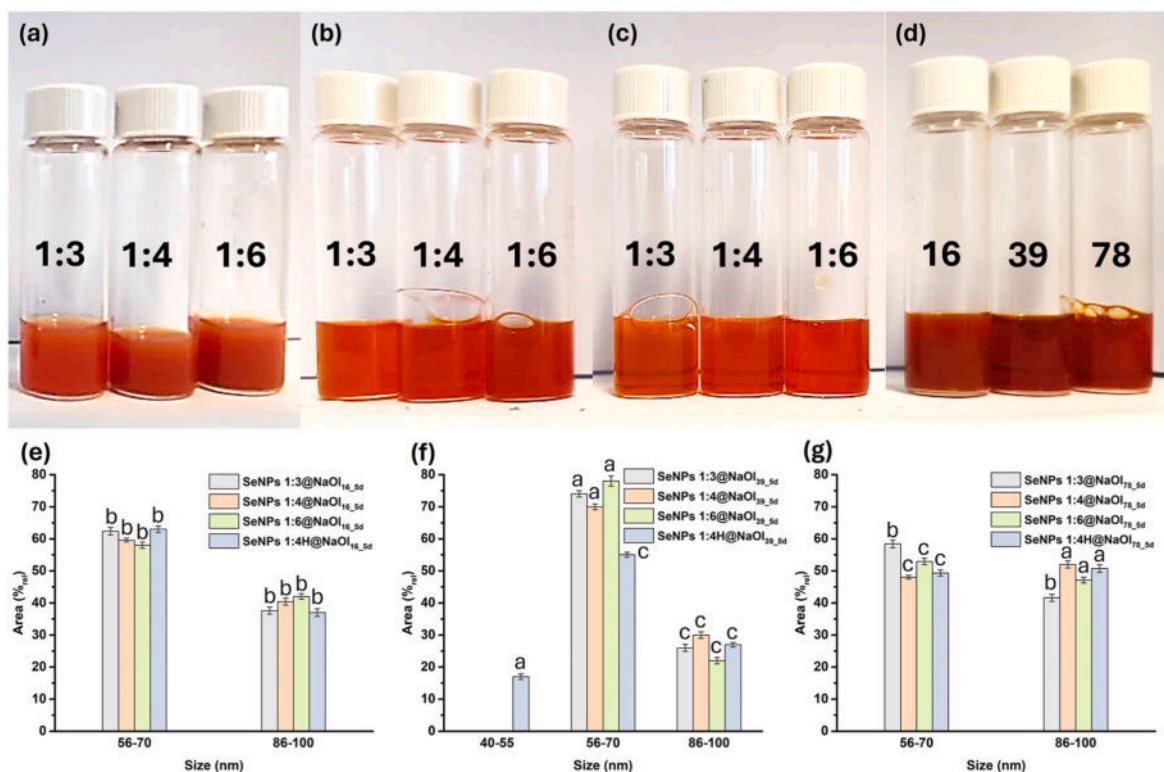

Fig. 9. Stability of SeNPs@NaOl dispersions over time. (**a-g**) SeNPs@NaOl stability over time monitored (**a-d**) macroscopically after two months from their synthesis and (**e-g**) using the implemented new model based on Mie's scattering theory to determine SeNP size evolution within 5 days-old dispersions. In the panels (**e-g**), the statistical significance of normalize integrals referring to each SeNP population (i.e., 40–55, 56–70, 71–85, 86–100 nm; independent variables) within SeNPs@NaOl obtained using either 16, 39, or 78 mM NaOl after 5 days from the synthesis was assessed through the one-way ANOVA analysis and the subsequent Tukey's Honestly Significant Difference (HSD) test. Different letters represent statistically different integrals ($p < 0.05$) from the largest value (*a*) to the smallest (*c*) one, except for the 40–55 nm NP population, which was observed only for SeNPs 1:4H@NaOl$_{39}$ after 5 days from the synthesis.

nm) increased during the considered timeframe, being more significant (A$_{rel} > 40$ %) for NPs obtained by using 16 or 78 mM NaOl. The outcome of the implemented model was in line with SEM imaging of aged SeNPs@NaOl dispersions (Fig. S15), which displayed NPs featuring 70 $\pm$ 8 nm, 62 $\pm$ 5 nm, and 82 $\pm$ 12 nm as average diameters when using 16, 39, or 78 mM NaOl for their synthesis, respectively.

ζ potential measurements, XPS, Raman and ATR-FTIR spectroscopies (Fig. 10) provided detailed information regarding the SeNP@NaOl stabilization. All NP dispersions featured ζ potential values < −30 mV

(Fig. 10a), confirming their electrostatic stability. The similarity between ζ potential trends of SeNPs@NaOl dispersions and the corresponding confined environments indicated that analogous electrostatic interactions occurred. Raman, XPS, and ATR-FTIR spectroscopies were performed solely focusing on SeNPs 1:4@NaOl to gain insights on substances within the dispersions and their interaction when the redox reaction was completed. SeNP crystal structure was assessed through Raman spectroscopy, which revealed contributions in the bond-bending vibrational mode (70-150 cm^{-1}) and Se–Se bond stretching vibrational
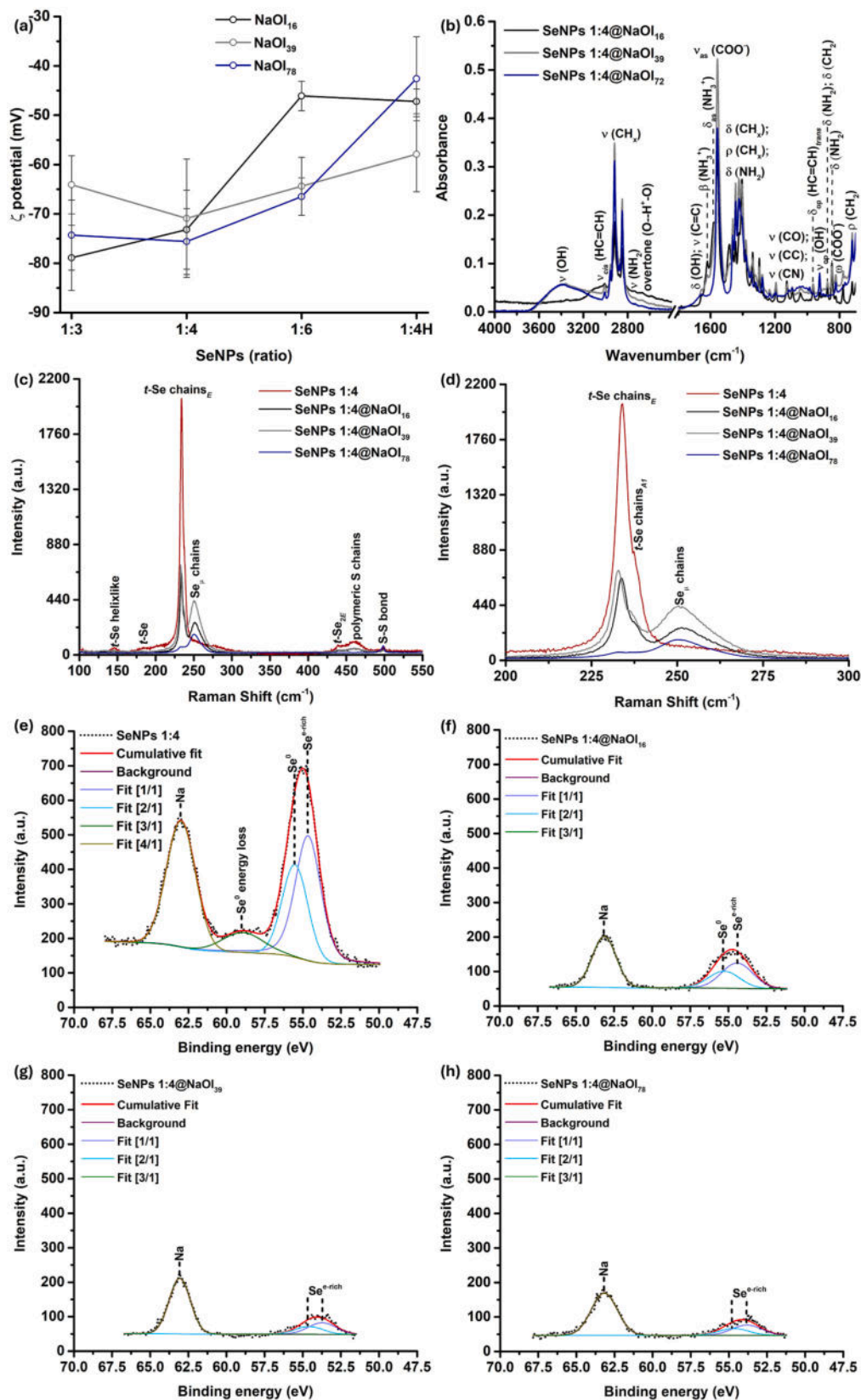
Fig. 10. Stability and crystallinity of SeNPs. (**a**) ζ potential measurements, (**b**) ATR-FTIR spectroscopy, (**c-d**) Raman spectroscopy, and (**e-h**) XPS analysis on fresh SeNP dispersions. ATR-FTIR, Raman, and XPS spectra were collected for SeNPs produced in water or C@NaOl confined environments by using the stoichiometric 1:4 ratio between Na_2SeO_3 and L-cysteine. For (**a**) ζ potential measurements, the one-way ANOVA analysis, and the subsequent Tukey's Honestly Significant Difference (HSD) test, revealed no statistically significant difference ($p > 0.05$) between SeNPs@NaOl dispersions. In (**e-h**) XPS spectra, binding energies for Na: 63.0–63.2 eV; binding energies for Se3d: Se^0 energy loss at 58.9 eV, Se^0 at 55.5–55.3 eV, and Se^{e-rich} at 54.7–54.4 eV and 53.8–53.7 eV.

mode (150-300 cm^{-1}) regions [30] for NPs produced in water and the C$_{24}$@NaOl environments (Fig. 10c–d; Table S12). Specifically, all SeNPs 1:4 dispersions displayed a signal at ca. 234 cm^{-1} typical of intrachain antisymmetric bond stretching of trigonal Se (*t*-Se) in *E* symmetry [31] alongside the S–S stretching peak at 499 cm^{-1}, attributable to RSSR molecules generated *via* redox reaction [32]. SeNP synthesis in confined environments determined the rising of the intrachain bond-stretching mode of disordered amorphous polymer Se-chains (Se$_{\mu}$) at 250 cm^{-1} and decreased signals of *t*-Se at ca. 234 cm^{-1} [33]. Furthermore, weak signals referring to bond-bending vibrations (182 cm^{-1}) and intrachain antisymmetric bond stretching with *2E* symmetry (279 cm^{-1}) of *t*-Se observed for SeNPs 1:4 in water disappeared for SeNPs 1:4@NaOl dispersions. Se$_{\mu}$ contributions became predominant for SeNPs 1:4@NaOl$_{78}$, which also showed the disappearance of the intrachain symmetric bond stretching with *A1* symmetry (shoulder at 237 cm^{-1}) [31] and intrachain antisymmetric bond stretching with *2E* symmetry (439 cm^{-1}) of *t*-Se, alongside the intrachain bond-stretching referring to polymeric sulphur chains (460 cm^{-1}). Spectral deconvolutions in the 200-300 cm^{-1} region (Fig. S16; Table S13) further confirmed the role of confined environments in limiting the transition from amorphous to trigonal Se within NPs. Indeed, normalized integrals referring to the former increased a function of the surfactant concentration at the expense of those related to *t*-Se. Moreover, spectral deconvolutions highlighted the appearance of a contribution at ca. 260 cm^{-1} typical of the generally unstable monomeric Se$_8$ rings (monoclinic Se) [30,33], which was the highest for SeNPs 1:4@NaOl$_{78}$ (Fig. S17). The mechanisms governing the stability of SeNPs in confined environments and the impaired transition from Se$_{\mu}$ to *t*-Se were evaluated through XPS and ATR-FTIR spectroscopy (Fig. 10b,e-h; Fig. S18; Table S14). XPS C1s spectra revealed contributions deriving from C–C/H bonds at 284.8 eV for all samples, whereas C–O binding energy shifted from 287.2 to 285.6 eV for SeNPs produced in water and C$_{24}$@NaOl environments (Fig. S18). Similarly, SeNPs 1:4 featured a signal at 288.7 eV attributable to O–C═O of L-cysteine, which downshifted up to 288.2 eV for SeNPs@-NaOl, being typical of C═O bonds of the surfactant. Furthermore, all samples displayed a contribution referring to Na at ca. 63 eV, which derived from Na$_2$SeO$_3$ and NaOl, and Se3d peaks as doublets in the 55.5–53.7 eV range (Fig. 10e–h). Deconvolutions of Se3d signals revealed the presence of the Se3d5/2 peak attributable to Se^0 (55.5–55.3 eV) only for SeNPs produced in water or the C$_{24}$@NaOl$_{16}$ confined environment (Fig. S18). Yet, this contribution was minor (as relative area) than that centred at 54.7 eV (Fig. S19), present in all SeNP samples, inferring an electron transfer from the reducing and stabilizing agents to Se atoms on the NP surface, which is indicated here as Se$^{e\text{-rich}}$ contribution [33]. Upon using 39 or 78 mM NaOl for SeNP synthesis, a Se3d contribution at ca. 53.8 eV arose, becoming the most represented relative area under these conditions (Figs. S18–S19). Moreover, SeNPs 1:4 displayed a peak at 58.9 eV, which is usually detected in combination with the Se^0 signal and is attributed to the energy loss of Se in its elemental state. IR spectra revealed vibrational modes typical of NaOl and cysteine-derived species (i.e., RSSR, RSOSR, and RSO$_2^-$), either as free residues or adsorbed on SeNP surfaces (Fig. 10b; Table S14). The IR absorbance of these species was particularly visible for contributions centred at 1295-1250, 1065, 985, and 875-730 cm^{-1} related to –CH$_2$, –CH, –OH, –CO, –NH$_2$, –NH$_3^+$, –CN, and –SO vibrations, which were more significant for SeNPs@NaOl$_{16}$ and SeNPs@NaOl$_{39}$ dispersions. Finally, variation in the peak position of these contributions or those referring to the hydrogen bond network (-OH stretching and O···H$^+$-O overtone) compared to C@NaOl environments or NPs in water inferred the interactions between NaOl, RSSR, RSOSR, and RSO$_2^-$ species that contributed to the overall SeNP stabilization.

4. Discussion

Combining the surfactant NaOl, whose C$_{18}$ chain provides good steric hindrance, and the amino acid L-cysteine, a convenient and safe

SeO$_3^{2-}$-reducing agent, allowed obtaining an easy, biocompatible, and cost-effective confined environment for synthesizing SeNPs, overcoming crucial issues related to pH conditions, yield, and NP stability typical of the synthesis in water.

A fundamental drawback of the latter process regards the natural tendency of amorphous (red) Se, typical of NPs obtained through redox processes, to transform into the stable trigonal (grey) Se forming 1D nano- and micro-structures [10,29]. This phenomenon can be prevented only by RSSR, RSO$_2$H, RSO$_2^-$, and RSOSR compounds (Fig. S4; Tables S4–S5) that can act as L- or X-type ligands coordinating with Se atoms on the NP surface [29], as also inferred by the Se$^{e\text{-rich}}$ contribution (54.7 eV) observed in the Se3d XPS spectrum of SeNPs 1:4 (Fig. 10e–h). In this regard, superoxide ions (O$_2^-$) or hydrogen peroxide (H$_2$O$_2$) formed during the process can oxidize cysteine to cysteine sulfenic acid (RSOH), which, in turn, either undergoes the same process generating RSO$_2$H and RSO$_2^-$ or reacts with itself, forming RSOSR [34–36]. Yet, electrostatic contributions are not sufficient to prevent the irreversible phase transition of Se atoms occurring within 24h from the NP synthesis (Fig. 3b). The exclusive presence of *t*-Se signals in the Raman spectrum of SeNPs 1:4 (Fig. 10c–d; Figs. S16–17) further corroborates this hypothesis, as the chosen experimental conditions (i.e., laser wavelength and power density) likely caused the ring-to-chain transition of Se (T = 50 °C) within NPs and its consequent photocrystallization [37]. Besides, variations in pH, SeO$_3^{2-}$:L-cysteine ratio, and precursor amounts can favour this transition. For instance, neutrality or alkaline conditions may cause the preferential formation of RSSR over RSO$_2^-$ or RSOSR [38], reducing the functional groups able to interact with the SeNP surface and generating irregular SeNPs, microaggregates, and crystals (Fig. 4 d-i). Alkaline conditions also delayed SeNP formation (Figs. S5c,f,i), as SeO$_3^{2-}$ and S$^-$-containing L-cysteine are mostly present [39], which, being less prone to interact than their acidic and protonated counterparts, slow the reaction rate. This phenomenon is mitigated at neutral pH [39]. Similarly, the L-cysteine excess (i.e., 1:6 ratio) likely adsorbed onto the SeNP surface, forming irregular aggregates (Fig. 4c), whereas increasing the precursor concentrations enhances the number of Se atoms in a small volume, improving the chances for Se-phase transition to occur.

In C@NaOl confined environments, spherical, regular, and small SeNPs are formed instantaneously in alkaline conditions, even when using L-cysteine excess and elevated precursor concentrations, without irreversible aggregation up to two months from their synthesis (Figs. 4 and 5a-d,7,8; Figs. S3 and S6). SeNP formation under alkaline conditions likely links to the anchoring of SeO$_3^{2-}$ and S$^-$-amino acid, the most represented species, provided by surfactant head groups through hydrogen bonds involving also water (Fig. 10b; Table S14). This dense hydrogen bond network confines SeNP precursors, increasing their local concentrations, facilitating the redox reaction even in alkaline conditions, and guaranteeing the proximity of Se atoms needed to generate NPs. The production of spherical and regular SeNPs, even when using 1:6 or 1:4H ratios, relied partially on the same hydrogen network. For instance, the anchoring of L-cysteine to NaOl head groups may slow down, or even hinder, the preferential formation of RSSR residues under alkaline conditions, leaving RSOSR and RSO$_2^-$ moieties available to interact with the SeNP surface, as observed in XPS and ATR-FTIR spectra (Fig. 10). Yet, SeNP formation and stabilization also depended on the aggregates within C@NaOl dispersions, which limited the amorphous-to-trigonal Se transition through electrostatic and steric repulsions and acted as NP templates, governing their size and shape. Overall, L-cysteine triggered the NaOl transition from spherical and/or ellipsoidal micelles to vesicles (L$_{\alpha L}$ phase) as indicated by the scattering contribution and d$_H$ values detected through UV–Visible spectroscopy and DLS measurements (Fig. 1a,b,e), respectively. This phenomenon derives from the electrostatic shielding of surfactant head groups and the hydrophobic effect exerted by its tails. When pH > pK$_{a\_NaOl}$ (ca. 8.0), salt-bridging interactions occurred between L-cysteine and NaOl (Figs. S1 and S2; table S3), varying the surfactant surface charge density and

forming a stabilized electric double layer (EDL). The latter entraps a high number of Na^+ in dispersions, drastically decreasing their conductivity and surface potential (Fig. 1d–f); yet, amino acidic -COO⁻ and -S⁻ groups (pK_a = 8.16) can contribute to this phenomenon. Additionally, pH values close to 8.0 favour intermolecular hydrogen bonds that stabilize NaOl head groups [40], as indicated by the appearance or the significant shift of the –OH stretching vibration (3370-3400 cm^{-1}; Fig. 2) typical of water molecules accepting hydrogen bonds and/or forming water clusters [41,42]. Ionic groups of L-cysteine also increase water entropy and modify the surfactant tail solubility [43], varying its physical-chemical makeup, as indicated by ATR-FTIR spectroscopy (Tables S2 and S3). Specifically, the disappearance or the shift of NaOl peaks referring to –CH_2 groups closed to the C_9-unsaturation and in *trans* configuration (1465-1315 cm^{-1}; Fig. S2) of C@NaOl dispersions [44,45] suggests a loss of all-*trans* conformation and packing in the modified triclinic O′$_{11}$ subcell in favour of a more mobile and fluid $L_{\alpha L}$ phase [44], confirming the hydrophobic effect of water on NaOl tails, which organize in vesicles. The C@NaOl confined environment is modulable for both vesicle amount and size, crucial parameters for SeNP production, as summarized in Fig. 11.

When L-cysteine falls short NaOl, few vesicles are formed (Fig. 11a), as the low amino acid concentration maintains a pH > 8.6 and limits salt bridging interactions, hydrogen bonds, and water entropy, favouring micellar aggregates, as indicated by DLS measurements for C@NaOl and NaOl colloids (Fig. 1e). Moreover, the κ $L_{\alpha L}/L_1$ phase ratios, which relate to the number of vesicle bilayers [46], calculated based on Fig. 1d are 0.63, 0.80, and 0.74 for 16, 39, and 78 mM NaOl, respectively, typical of one-bilayer and similar vesicles. The constant κ regions (Fig. 1d) and PdI values (Table S1) observed under this scenario suggest that vesicles are stable in size. This outcome may derive from the limited L-cysteine coating around the surfactant heads and subsequent low Na^+ dissociation. κ ratios, alongside PdI values, remain constant until NaOl: L-cysteine is ca. 2, suggesting the requirement of an amino acid threshold concentration for modifying these aggregates. C@NaOl$_{78}$ dispersions represent a magnification of this scenario, as for most of the explored conditions [L-cysteine] < [NaOl]. Besides, although vesicle formation affected ζ potential similarly to conductivity, the former is influenced by the amino acid speciation; at pH ≥ 9, almost all amino acid –SH are deprotonated, determining a significant drop in the dispersion surface

charge, with a greater extent for 78 mM than 39 mM NaOl (Fig. 1c and d). The mixture of NaOl micelles and few C@NaOl vesicles within this scenario makes the confined environment not uniform, causing a disordered anchoring of L-cysteine and SeO_3^{2-} on the NaOl surface, poor control over the redox reaction, and a high polydispersity of the formed SeNPs (Fig. 6b,c, 8, and 10d; Table S8). XPS analysis sustains this evidence, as SeNP 1:4 dispersions produced with [L-cysteine] < [NaOl] showed two Se^{e-rich} contributions (Fig. 10e–h; Fig. S19) likely derived from different electron transfer from the NaOl micelles and C@NaOl vesicles - X- and L-type ligands - to the SeNP surface, improving the electron richness of Se coordination sites. In turn, the highest coordination between Se atoms on the NP surface and surfactant-containing aggregates in SeNPs 1:4@NaOl$_{39}$ and SeNPs 1:4@NaOl$_{78}$ can limit the transition from Se_μ and Se_8 rings to t-Se, aligning with Raman spectroscopy results (Fig. S17; table S13) and previous studies [33]. In this regard, the detection of Raman shifts typical of Se_8 rings (ca. 260 cm^{-1}) within these dispersions infers the good stabilizing activity of NaOl micelles and C@NaOl vesicles on Se, as this phase generally undergoes rapid transformation under heat or illumination [37]. The variance in Se_μ, t-Se, and Se_8 integrals (as relative area) observed in Raman spectra of these SeNP dispersions may relate to their different size distribution of NPs, as SeNPs 1:4@NaOl$_{39}$ displayed less polydisperse and bigger NPs than SeNPs 1:4@NaOl$_{78}$ (Fig. 6b and c). Indeed, the ring-to-chain transition of Se might be favoured within bigger NPs than smaller ones, as the higher amount of Se atoms in the former are more likely to interact with each other. Although confined environments with an amino acid deficiency efficiently limit Se crystallization, they cannot prevent the NP evolution and aggregation over time. Indeed, the population of small (40–55 nm) NPs evolved over the 5-day incubation, becoming part of the one featuring 56–70 nm as the average diameter (Fig. 9f and g). This outcome directly correlates with the elevated number of NaOl micelles within these NP dispersions that, due to their small size, can limitedly counteract NP aggregation due to short-range interactions [2], exerting a scarce steric hindrance, alongside the alkaline pH conditions, which favour the formation of less interacting RSSR residues than oxidized ones [38] (Fig. 10b; Table S14). In turn, SeNPs can undergo an Ostwald-ripening mechanism, according to which the smallest NPs – i.e., the most soluble – dissolve, and the available Se atoms adsorbed onto the surface of bigger NPs, generating less
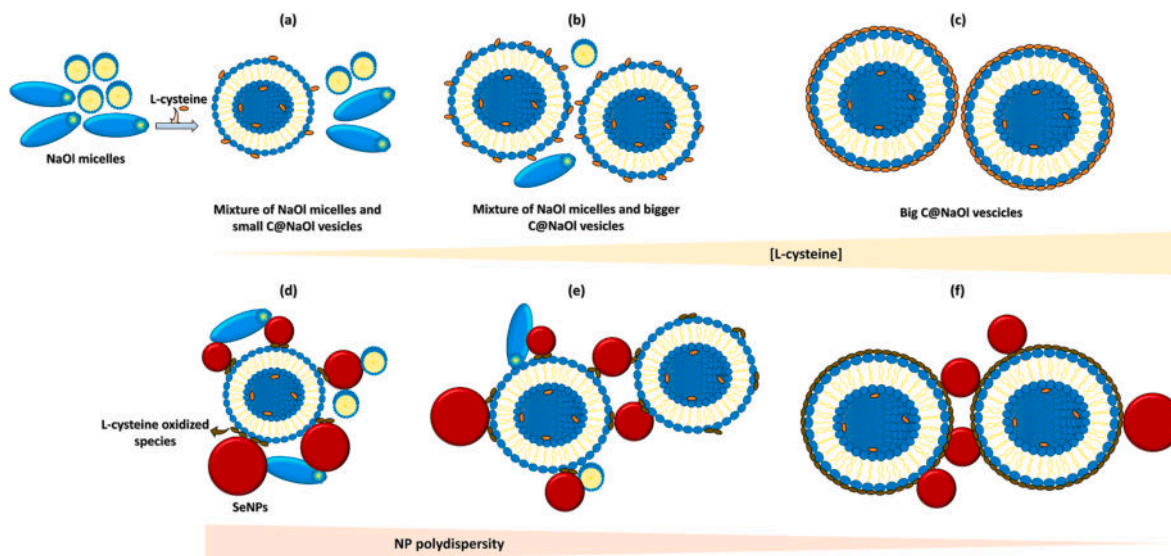

Fig. 11. Modulability of C@NaOl confined environments and their impact on SeNP synthesis. (**a**) A defect of L-cysteine compared to NaOl generates few and small C@NaOl vesicles and maintains surfactant micelles, which, in turn, (**d**) limitedly controlled the rate of SeNP formation and growth through Ostwald ripening. (**b**) When L-cysteine and NaOl concentration are similar, more and bigger C@NaOl vesicles and (**e**) less polydisperse SeNPs are formed, due to the higher steric hindrance exerted by these aggregates than NaOl micelles. (**c**) An excess of L-cysteine enables obtaining the most uniform confined environment consisting of big C@NaOl vesicles that simultaneously control the NP rate and yield and (**f**) electrosterically stabilize SeNPs, which became more regular in size.

polydisperse populations. Most SeNPs were also smaller in size than those obtained when L-cysteine exceeds NaOl (Figs. 6 and 8; Table S8), likely due to the numerous NaOl micelles that confined SeO_3^{2-} and L-cysteine in various locations, limiting the chances for an elevated number of Se atoms to encounter and form big SeNPs.

When the amino acid and surfactant amounts are comparable, salt bridging interactions are favoured rather than the previous scenario, as indicated by the rising of several $-NH_3^+$ vibrational modes in $C_{72}@NaOl_{78}$ dispersions, particularly regarding its deformation (Table S2; Fig. S2), whose high integral relates to the absence of free amino acid that could hinder signal detection. Yet, d_H values of $C_{36}@NaOl_{39}$ and $C_{72}@NaOl_{78}$ are comparable to those of surfactant colloids (Fig. 1e), indicating the formation of a few vesicles. In these conditions, κ and ζ potential measurements suggest that L-cysteine-NaOl interaction mediates the vesicle enlargement (Fig. 1d–f; 11b). The increased salt bridging determines an enhanced amino acid coating on the surfactant head groups that can improve Na^+ dissociation in the medium and, hence, conductivity and surface charge. In this scenario, the amino acid steric hindrance towards the surfactant becomes more significant and is partially responsible for the vesicle's increased size. Even water entropy improves, triggering a more pronounced effect on surfactant tails than when NaOl is in excess. In this regard, $C_{72}@NaOl_{78}$ dispersion displayed the most fluid $L_{\alpha L}$ phase (Fig. S2), indicating a more substantial rearrangement of hydrophobic NaOl tails in the former responsible for the vesicle's enlargement. Regardless of these peculiarities, SeNPs 1:6@NaOl$_{39}$ and SeNPs 1:4H@NaOl$_{78}$ showed size distributions similar to those obtained when NaOl exceeded L-cysteine (Figs. 6 and 8; Table S8), corroborating the importance of vesicles for NP physical-chemical features. The vesicle enlargement becomes crucial when considering the SeNP stability over time, as these dispersions displayed the highest integrals (ca. 80 % and 60 %) referring to 56–70 nm SeNPs after 5 days of incubation within those obtained by using 39 or 78 mM NaOl (Fig. 9f and g). In this regard, large vesicles, although limited in number, exert a marked steric hindrance, which can better overcome Se tendency to aggregate to reach its thermodynamic equilibrium (Fig. 11e).

An excess of L-cysteine further improves salt bridging with NaOl, increasing the production of vesicles and their enlargement (Fig. 11c), as inferred by the distinguishable and greater d_H values for C@NaOl$_{16}$ and $C_{72}@NaOl_{39}$ dispersions than the NaOl counterparts (Fig. 1e). The $C_{72}@NaOl_{39}$ system features a larger d_H (ca. 360 nm) than C@NaOl$_{16}$ dispersions, attributable to the more fluid $L_{\alpha L}$ phase of the former (Fig. S2). Instead, the amino acid excess in C@NaOl$_{16}$ dispersions forms a shell surrounding the surfactant head groups, which can better stabilize NaOl vesicles through hydrogen bonds (Fig. 2; Table S2), making the overall structure more rigid. In this regard, $C_{72}@NaOl_{16}$ dispersion displayed less IR stretching contributions of amino acid $-NH_3^+$ groups and a higher number of vibrational modes typical of L-cysteine not interacting with NaOl than the other systems (Fig. S2; Tables S2 and S3). Despite differences between C@NaOl$_{16}$ and $C_{72}@NaOl_{39}$ dispersions, vesicles formed in these conditions seem stable in size, being more evident for the former from d_H, κ, and ζ potential values (Fig. 1d–f; Table S1), suggesting that once a threshold number of vesicles is formed, L-cysteine in excess stabilizes them (ca. 220 nm). Specifically, the less negative surface charge of C@NaOl$_{16}$ dispersion (Fig. 1f) reflects the amino acid speciation, whose $-SH$ groups increase at expenses of $-S^-$ moieties as the pH becomes closer or below its pK_a (8.16) [39], and the interaction between $-COO^-$ and $-NH_3^+$ groups of NaOl and L-cysteine, respectively. This phenomenon, more distinguishable at low surfactant concentration, significantly lowers the number of free negatively charged carboxylate moieties and increases the amount of free Na^+ counterions in the dispersion. Similar conclusions can be drawn from conductivity and surface charge measurements for $C_{72}@NaOl_{39}$ dispersions. Nevertheless, the less negative ζ potential value observed for the $C_{72}@NaOl_{16}$ system likely links to the presence of $-SH$ groups and a portion of acidic NaOl $-COOH$ moieties, as the pH < 8.0 for this

dispersion, decreasing the head group repulsion and increasing the packing of hydrophobic moieties [47], hence their rigidity, as observed through ATR-FTIR spectroscopy (Fig. S2). The increased number of C@NaOl vesicles reflects the low polydispersity and high stability over time of SeNPs@NaOl$_{16}$ and SeNPs 1:4H@NaOl$_{39}$ (Fig. 6a and b and 9e,f; Table S8). Indeed, when vesicles are predominant, the confined environment is homogeneous and the amino acid molecules form a shell around NaOl head groups, as also indicated by the similarity between XPS spectra and contributions of SeNPs 1:4@NaOl$_{16}$ and SeNPs 1:4 (Fig. 10c and d; Fig. S19), which inferred that a similar degree of electron transfer from the capping agents to the NP surface occurred within these dispersions, also in line with previous reports [33]. Nevertheless, the $C_{24}@NaOl_{16}$ confined environment partially limited the Se_μ-to–t-Se transition (Fig. 10c and d; Fig. S17; table S13) than the synthesis in water, likely due to the good control exerted by the C@NaOl aggregates over the NP size. Indeed, these aggregates, being bigger than 200 nm, provide good steric and electrostatic hindrance, enabling to obtain smaller SeNPs than those in water (Fig. 8a; Fig. S3) and prevent their encountering and agglomeration (Fig. 11f). In this regard, SeNPs@NaOl$_{16}$ always displayed two UV–Visible contributions referring to 56–70 nm (Area$_{\%rel}$ > 70 %) and the less representative 86–100 nm SeNPs, agreeing with Olutas' work [2]. The same NP populations were also detected after 5-day incubation, although the contribution of big NPs slightly increased (ca 40 %), likely due to their partial ripening. Similarly, the smallest NP population (40–55 nm) was maintained over time only in the SeNPs 1:4H@NaOl$_{39}$ dispersion, the most stable among those investigated here (Fig. S14). The steric contribution avoiding NP aggregation was enhanced for the latter dispersion, as the $C_{72}@NaOl_{39}$ system featured bigger vesicles than those obtained for C@NaOl$_{16}$ colloids (Fig. 1d).

4.1. SeNP size determination

Size is a key parameter for nanomaterials, as it dictates several of their physical-chemical and applicative properties, making it imperative to have reliable, cost-effective, rapid, and easy methods to determine this feature. DLS measurements and the Tauc-plot method are generally used for this purpose, sometimes even disregarding their intrinsic limitations. For instance, the former becomes ineffective when NPs are not spherical, stabilized by auto-assembled aggregates with different size and morphology, and/or when the stabilizer concentration exceeds that of NPs, as the estimated d_H refers to the diameter of a sphere capable of scattering the light in liquid medium like colloids within the samples [48]. Indeed, DLS measurements overestimated SeNP size either in water or in C@NaOl environment due to cystine crystals, cysteine excess, NaOl micelles, and C@NaOl vesicles within the dispersions (Table S7). Similarly, the Tauc-plot method is vastly used for NP size determination, yet its applicability and validity strongly depend on the material and the correct determination of its E_g. Although an in-depth discussion of this topic is beyond the scope of this work, the spectral overlap of different bands, absorption (Urbach) tails, and excitons [49] can affect the E_g determination for Se. Indeed, the latter, even as bulk, features five local valence and conduction bands deriving from the short-range-ordered energy states, which lead to a broad absorption spectrum where these contributions overlap [50,51]. In turn, this outcome causes defect states close to the band edges that, alongside impurities, phonons, and excitons, contribute to the arising of Urbach tails [49,50]. Specifically, excitons dominate the Se-absorption edge at room temperature, determining significant shifts in its absorption edge and broadening its spectrum [43]. Se scaling down to the nanorange emphasizes these phenomena, as indicated by UV–Visible spectra of SeNPs in water or C@NaOl dispersions (Figs. 3c and 5e,g,i), making their E_g and size determination through the Tauc-plot model inaccurate. On the opposite, assimilating exciton resonance and transition of SeNPs with surface plasmon resonance of metal-based NPs allowed us to implement a new method for determining SeNP size based on Mie's

scattering theory, which was reliable for 40–100 nm SeNPs (Fig. 8). Indeed, UV–Visible spectra simulations for SeNPs bigger than 100 nm showed absorption contributions that did not linearly correlate with the simulated size (Fig. S7) and close, in peak position and broadening, to those of bulk Se [7], in line with the definition of nanoparticle per sè. Instead, SeNPs smaller than 40 nm did not feature scattering contributions, likely due to the significant difference between d_{SeNP} and the incident wavelength, the domination of dipole absorption over dipole scattering, and a rearrangement of electrons between the NP surface and the medium [52–54]. Nevertheless, the developed method can easily, rapidly, and inexpensively determine the size of SeNPs in a range typical of NPs obtained through reduction methods [6], proving its usefulness and validity.

5. Conclusions

Our study successfully addresses critical challenges associated with SeNP synthesis by introducing a novel confined environment utilizing the surfactant sodium oleate (NaOl) and the amino acid ʟ-cysteine. This approach offers a bio-compatible, cost-effective, and versatile platform for the controlled synthesis of SeNPs, overcoming various challenges associated with traditional water-based synthesis methods. Leveraging the unique properties of NaOl and ʟ-cysteine (e.g., steric hindrance, redox activity, and their salt-bridging interaction) within confined environments enables the instantaneous production of spherical, regular, and small (40–70 nm) SeNPs, even under alkaline ($9.6 < pH < 7.6$) conditions. Electrosteric contributions within the C@NaOl environments and the coordination of Se atoms with functional groups of these dispersions limited the amorphous-to-trigonal phase transition of selenium, improving its stability at room temperature, and increased up to 3-fold the yield of SeNPs without aggregation. Furthermore, C@NaOl dispersions proved modulable for vesicle formation, as an amino acid excess or defect enabled obtaining vesicles (ca 200–300 nm) or a mixture of polydisperse NaOl micelles and C@NaOl vesicles. In turn, these aggregates influenced SeNP size and stability over time. Using a mixture of micelles and vesicles led to smaller (40–55 nm) yet less stable and more polydisperse SeNPs. Instead, the predominant presence of vesicles increased SeNP stability and decreased their polydispersity; yet these NPs were bigger (56–70 nm) than those obtained when ʟ-cysteine fell short NaOl. Lastly, we introduce a novel method based on Mie's scattering theory for accurate SeNP size determination (validity range: 40–100 nm) as a reliable alternative to traditional techniques like dynamic light scattering (DLS) and the Tauc-plot method, adding a valuable tool to the characterization toolbox of SeNPs.

Thus, this study underscores the significance of tailored confined environments for synthesizing SeNPs and the potential manipulation of their size, morphology, and stability through precise control over the synthesis parameters, offering promising prospects for various technological applications.

Funding sources

CRediT authorship contribution statement

Elena Piacenza: Writing – original draft, Visualization, Validation, Methodology, Investigation, Formal analysis, Data curation, Conceptualization. **Filippo Vitale:** Validation, Formal analysis, Data curation. **Veronica Ciaramitaro:** Validation, Formal analysis. **Renato Lombardo:** Writing – review & editing, Data curation. **Francesco Ferrante:** Writing – review & editing, Supervision. **Delia F. Chillura Martino:** Writing – review & editing, Supervision, Resources, Funding acquisition, Conceptualization.

Declaration of competing interest

The authors declare that they have no known competing financial interests or personal relationships that could have appeared to influence the work reported in this paper.

Data availability

Data will be made available on request.

Acknowledgements

Appendix B. Supplementary data

Supplementary data to this article can be found online at https://doi.org/10.1016/j.mtchem.2024.102115.

References

[1] M.M. El-Kady, et al., Nanomaterials: a comprehensive review of applications, toxicity, impact, and fate to environment, J. Mol. Liq. 370 (2023) 121046, https://doi.org/10.1016/j.molliq.2022.121046.

[2] E.B. Olutas, Alkyl chain length and headgroup dependent stability and agglomeration properties of surfactant-assisted colloidal selenium nanoparticles, Colloids Surf., A: Physicochem. Eng. 661 (2023) 130935, https://doi.org/10.1016/j.colsurfa.2023.130935.

[3] S. Shrestha, B. Wang, P. Dutta, Nanoparticle processing: Understanding and controlling aggregation, Adv. Colloid Interface Sci. 279 (2020) 102162, https://doi.org/10.1016/j.cis.2020.102162.

[4] T. Song, et al., A review of the role and mechanism of surfactants in the morphology control of metal nanoparticles, Nanoscale 13 (2021) 3895–3910, https://doi.org/10.1039/D0NR07339C.

[5] E. Piacenza, A. Presentato, R.J. Turner, Stability of biogenic metal(loid) nanomaterials related to the colloidal stabilization theory of chemical nanostructures, Crit. Rev. Biotechnol. 38 (2018) 1137–1156, https://doi.org/10.1080/07388551.2018.1440525.

[6] N. Bisht, P. Phalswal, P.K. Khanna, Selenium nanoparticles: a review on synthesis and biomedical applications, Mat, Adv 3 (2022) 1415–1431, https://doi.org/10.1039/D1MA00639H.

[7] E. Piacenza, A. Presentato, B. Heyne, R.J. Turner, Tunable photoluminescence properties of selenium nanoparticles: biogenic versus chemogenic synthesis, Nanophotonics 9 (2020) 3615–3628, https://doi.org/10.1515/nanoph-2020-0239.

[8] E. Piacenza, A. Presentato, E. Zonaro, S. Lampis, G. Vallini, R.J. Turner, Selenium and tellurium nanomaterials, Phys. Sci. Rev. 3 (2018) 20170100, https://doi.org/10.1515/psr-2017-0100.

[9] Y. Huang, Q. Chen, H. Zeng, C. Yang, C. Wang, L. Zhou, A review of Selenium (Se) nanoparticles: from synthesis to applications, Part. Part, Syst. Charact. 40 (2023) 2300098, https://doi.org/10.1002/ppsc.202300098.

[10] Y. Wu, Y. Ni, Low temperature rapid preparation of selenium nanoparticles in the presence of food surfactants, Chem. Eng. J. 187 (2012) 328–333, https://doi.org/10.1016/j.cej.2012.01.075.

[11] S.K. Mehta, S. Chaudhary, K.K. Bhasin, Understanding the role of hexadecyltrimethylammonium bromide in the preparation of selenium nanoparticles: a spectroscopic approach, J. Nanopart. Res. 11 (2009) 1759–1766, https://doi.org/10.1007/s11051-008-9542-5.

[12] V. Bartunek, et al., Preparation of amorphous antimicrobial selenium nanoparticles stabilized by odor suppressing surfactant polysorbate 20, Mat. Lett. 152 (2015) 207–209, https://doi.org/10.1016/j.matlet.2015.03.092.

[13] S. Gangadoo, D. Stanley, R.J. Hughes, R.J. Moore, J. Chapman, The synthesis and characterization of highly stable and reproducible selenium nanoparticles, Inorg. Nano-Met. 47 (2017) 1568–1576, https://doi.org/10.1080/24701556.2017.1357611.

[14] S. Chaudhary, P. Chauhan, R. Kumar, K.K. Bhasin, Toxicological responses of surfactant functionalized selenium nanoparticles: a quantitative multi-assay approach, Sci. Total Environ. 643 (2018) 1265–1277, https://doi.org/10.1016/j.scitotenv.2018.06.296.

[15] P. Chauhan, S. Chaudhary, Role of surface modification on selenium nanoparticles: Enumerating the optical, thermal and structural properties, Opt. Mat. 97 (2019) 109380, https://doi.org/10.1016/j.optmat.2019.109380.

[16] J. Huang, W. Huang, Z. Zhang, X. Lin, H. Lin, L. Peng, T. Chen, Highly uniform synthesis of selenium nanoparticles with EGFR targeting and tumor microenvironment-responsive ability for simultaneous diagnosis and therapy of nasopharyngeal carcinoma, ACS Appl. Mater. Interfaces 11 (2019) 1177–1193, https://doi.org/10.1021/acsami.8b22678.

[17] X. Cao, et al., Tuning self-assembly of amphiphilic sodium alginate-decorated selenium nanoparticle surfactants for antioxidant Pickering emulsion, Int. J. Biol. Macromol. 210 (2022) 600–613, https://doi.org/10.1016/j.ijbiomac.2022.04.214.

[18] A. Blinov, et al., Synthesis and characterization of selenium nanoparticles stabilized with cocamidopropyl betaine, Sci. Rep. 12 (2022) 21975, https://doi.org/10.1038/s41598-022-25884-x.

[19] S. Cao, et al., Insights into the influence of temperature on the adsorption behavior of sodium oleate and its response to flotation of quartz, Int. J. Min. Sci. Technol. 32 (2022) 399–409, https://doi.org/10.1016/j.ijmst.2021.12.006.

[20] E. Piacenza, K. Sule, A. Presentato, F. Wells, R.J. Turner, E.J. Prenner, Impact of biogenic and chemogenic selenium nanoparticles on model eukaryotic lipid membranes, Langmuir 39 (2023) 10406–10419, https://doi.org/10.1021/acs.langmuir.3c00718.

[21] Q. Li, T. Chen, F. Yang, J. Liu, W. Zheng, Facile and controllable one-step fabrication of selenium nanoparticles assisted by L-cysteine, Mat. Lett. 64 (2010), https://doi.org/10.1016/j.matlet.2009.12.01, 614-417.

[22] K. Suga, D. Kondo, Y. Otuska, Y. Okamoto, H. Umakoshi, Characterization of aqueous oleic acid/oleate dispersions by fluorescent probes and Raman spectroscopy, Langmuir (2016) 327606–327612, https://doi.org/10.1021/acs.langmuir.6b02257.

[23] N. Dharaiya, U. Patel, V.K. Aswal, N.V. Sastry, B. Pratap, Different pH triggered aggregate morphologies in sodium oleate-cationic surfactants mixed systems, New J. Chem. 41 (2017) 9142–9151, https://doi.org/10.1039/C6NJ03871A.

[24] J. Oberdisse, O.G. Regev, Porte, Experimental study of the micelle-to-vesicle transition, J. Phys. Chem. B 102 (1998) 1102–1108, https://doi.org/10.1021/jp972390q.

[25] L. Zhai, X. Tan, Y. Chen, X. Huang, Influence of salt and polymer on the critical vesicle concentration in aqueous mixture of zwitterionic/anionic surfactants, Colloids Surf., A: Physicochem. Eng. 276 (2006) 28–33, https://doi.org/10.1016/j.colsurfa.2005.09.043.

[26] M. Gradzielski, M. Muller, M. Bergmeier, H. Hoffmann, E. Hoinkis, Structural and macroscopic characterization of a gel phase of densely packed monodisperse, unilamellar vesicles, J. Phys. Chem. B 103 (1999) 1416–1424, https://doi.org/10.1021/jp9833303.

[27] B. Yang, et al., Differential adsorption of hydrolytic polymaleic anhydride as an eco-friendly depressant for the selective flotation of apatite from dolomite, Sep. Pur. Technol. 256 (2021) 117803, https://doi.org/10.1016/j.seppur.2020.117803.

[28] M. Wolper, P. Hellwig, Infrared spectra and molar absorption coefficients of the 20 alpha amino acids in the spectral range from 1800 to 1500 cm^{-1}, Spectrochim. Acta Mol. Biomol. Spectrosc. 64 (2006) 987–1001, https://doi.org/10.1016/j.saa.2005.08.025.

[29] E. Piacenza, A. Presentato, F. Ferrante, G. Cavallaro, R. Alduina, D.F. Chillura Martino, Biogenic selenium nanoparticles: a fine characterization to unveil their thermodynamic stability, Nanomaterials 11 (2021) 1195, https://doi.org/10.3390/nano11051195.

[30] S.N. Yannopoulos, K.S. Andrikopoulos, Raman scattering study on structural and dynamical features of noncrystalline selenium, J. Chem. Phys. 121 (2004) 4747, https://doi.org/10.1063/1.1780151.

[31] V.V. Poborchii, A.V. Kolobov, K. Tanaka, An in situ Raman study of polarization-dependent photocrystallization in amorphous selenium films, Appl. Phys. Lett. 72 (1998) 1167, https://doi.org/10.1063/1.121002.

[32] X. Zhang, B. Yang, W. Zhou, Z. Zhu, Y. Bian, R. Zeng, Dynamic detection of thiol oxidation/reduction status during the conversion of cysteine/cystine, J. Mol. Struct. 1250 (2022) 131675, https://doi.org/10.1016/j.molstruc.2021.131675.

[33] K. Li, et al., Amorphous structure and crystal stability determine the bioavailability of selenium nanoparticles, J. Haz. Mat. 465 (2024) 133287, https://doi.org/10.1016/j.jhazmat.2023.133287.

[34] J. Kessi, K.W. Hanselmann, Similarities between the abiotic reduction of selenite with glutathione and the dissimilatory reaction mediated by Rhodospirillum rubrum and Escherichia coli, J. Biol. Chem. 279 (2004) 50662–50669, https://doi.org/10.1074/jbc.M405887200.

[35] D. Luo, S.W. Smith, B.D. Anderson, Kinetics and mechanism of the reaction of cysteine and hydrogen peroxide in aqueous solution, J. Pharm. Sci. 94 (2005) 304–316, https://doi.org/10.1002/jps.20253.

[36] J.P. Chauvin, D.A. Pratt, On the reactions of thiols, sulfenic acids, and sulfinic acids with hydrogen peroxide, Angew. Chem. Int. Ed. 56 (2017) 6255–6259, https://doi.org/10.1002/anie.201610402.

[37] W. Lu, et al., Structure of amorphous selenium: small ring, big controversy, J. Am. Chem. Soc. 146 (2024) 6345–6351, https://doi.org/10.1021/jacs.4c00219.

[38] J. Eidenschink, S. Bagherimetkazini, F.M. Matysik, Investigation of the electrochemical behavior of cysteine by hypenation of electrochemistry and mass spectrometry, Monatsh. Chem. 153 (2022) 775–780, https://doi.org/10.1007/s00706-022-02943-7.

[39] F. Gennari, V.K. Sharma, M. Pettine, L. Campanella, F.J. Millero, Reduction of selenite by cysteine in ionic media, Geochim. Cosmochim. Acta 124 (2014) 98–108, https://doi.org/10.1016/j.gca.2013.09.019.

[40] L. Guo, X. Guo, Y. Xia, Self-assembled vesicles of sodium oleate and chitosan quaternary ammonium salt in acidic or alkaline aqueous conditions, Colloid Polym. Sci. 297 (2019) 1455–1463, https://doi.org/10.1007/s00396-019-04571-w.

[41] P. Enev, P. Sedlacek, S. Jarabkova, T. Velcer, M. Pekar, ATR-FTIR spectroscopy and thermogravimetry characterization of water in polyelectrolyte-surfactant hydrogels, Colloids Surf., A: Physicochem. Eng. 575 (2019) 1–9, https://doi.org/10.1016/j.colsurfa.2019.04.089.

[42] Y. Ikemoto, et al., Infrared spectra and hydrogen-bond configurations of water molecules at the interface of water-insoluble polymers under humidified conditions, J. Phys. Chem. B 126 (2022) 4143–4151, https://doi.org/10.1021/acs.jpcb.2c01702.

[43] S.E. Maurer, G. Nguyen, Prebiotic vesicle formation and the necessity of salts, Orig. Life Evol. Biosph. 46 (2016) 215–222, https://doi.org/10.1007/s11084-015-9476-8.

[44] J.J. Kellar, C.A. Young, K. Knutson, J.D. Miller, Thermotropic phase transition of adsorbed oleate species at a fluorite surface by in situ FT-IR-IRS spectroscopy, J. Colloid Interf. Sci. 144 (1991) 381–389, https://doi.org/10.1016/0021-9797(91)90404-V.

[45] J.J. Najera, Phase transition behavior of sodium oleate aerosol particles, Atmosph. Environ. Times 41 (2007) 1041–1052, https://doi.org/10.1016/j.atmosenv.2006.09.016.

[46] H. Hoffmann, C. Thunig, P. Schmiedel, U. Munkert, Gels from surfactant solutions with densely packed multilamellar vesicles, Faraday Discuss 101 (1995) 319–333, https://doi.org/10.1039/FD9950100319.

[47] M. Jain, S. Kumar, V.K. Aswal, A. Al-Ghamdi, S.K. Kailasa, N.I. Malek, Amino acid induced self-assembled vesicles of choline oleate: pH responsive nano-carriers for targeted and localized delivery of doxorubicin for breast cancer, J. Mol. Liq. 360 (2022) 119517, https://doi.org/10.1016/j.molliq.2022.119517.

[48] A. Kim, W.B. Ng, W. Bernt, N.J. Cho, Validation of size estimation of nanoparticle tracking analysis on polydisperse macromolecule assembly, Sci. Rep. 9 (2019) 2639, https://doi.org/10.1038/s41598-019-38915-x.

[49] J. Klein, L. Kampermann, B. Mockenhaupt, M. Behrens, J. Strunk, G. Bacher, Limitations of the Tauc plot method, Adv. Funct. Mat. 33 (2023) 2304523, https://doi.org/10.1002/adfm.202304523.

[50] M. Saleh, M.M. Abdul-Gader Jafar, B.N. Bulos, T.M.F. Al-Daraghmeh, Determination of optical properties of undoped amorphous Selenium (a-Se) films by dielectric modelling of their normal-incidence transmittance spectra, Appl. Phys. Res. 6 (2014) 10–44, https://doi.org/10.5539/apr.v6n6p10.

[51] K.J. Siemens, E.W. Fenton, Optical absorption by excitons in amorphous selenium, Phys. Rev. 161 (1967) 632–636, https://doi.org/10.1103/PhysRev.161.632.

[52] X. Fan, W. Zheng, D.J. Singh, Light scattering and surface plasmons on small spherical particles, Light Sci. Appl. 3 (2014) e179, https://doi.org/10.1038/lsa.2014.60.

[53] U. Kreibig, M. Vollmer, Optical Properties of Metal Clusters, Springer-Verlag, Berlin, 1995, https://doi.org/10.1007/978-3-662-09109-8.

[54] K.P. Charle, L. Konig, S. Nepijko, I. Robin, W. Schulz, The surface plasmon resonance of free and embedded Ag clusters in the size range 1,5 nm < D < 30 nm, Cryst. Res. Technol. 33 (1998) 1085–1096, https://doi.org/10.1002/(SICI)1521-4079(199810)33:7/8%3C1085::AID-CRAT1085%3E3.0.CO;2-A.